Data Augmentation in High Dimensional Low Sample Size Setting Using a Geometry-Based Variational Autoencoder

Clément Chadebec, Elina Thibeau-Sutre, Ninon Burgos, Stéphanie Allassonnière

Data Augmentation in High Dimensional Low Sample Size Setting Using a Geometry-Based Variational Autoencoder

Clément Chadebec, Elina Thibeau-Sutre, Ninon Burgos, and Stéphanie Allassonnière, for the Alzheimer's Disease Neuroimaging Initiative, and the Australian Imaging Biomarkers and Lifestyle flagship study of ageing

Abstract—In this paper, we propose a new method to perform data augmentation in a reliable way in the High Dimensional Low Sample Size (HDLSS) setting using a geometry-based variational autoencoder. Our approach combines a proper latent space modeling of the VAE seen as a Riemannian manifold with a new generation scheme which produces more meaningful samples especially in the context of small data sets. The proposed method is tested through a wide experimental study where its robustness to data sets, classifiers and training samples size is stressed. It is also validated on a medical imaging classification task on the challenging ADNI database where a small number of 3D brain MRIs are considered and augmented using the proposed VAE framework. In each case, the proposed method allows for a significant and reliable gain in the classification metrics. For instance, balanced accuracy jumps from 66.3% to 74.3% for a *state-of-the-art* CNN classifier trained with 50 MRIs of cognitively normal (CN) and 50 Alzheimer disease (AD) patients and from 77.7% to 86.3% when trained with 243 CN and 210 AD while improving greatly sensitivity and specificity metrics.

1 Introduction

Even though always larger data sets are now available, the lack of labeled data remains a tremendous issue in many fields of application. Among others, a good example is healthcare where practitioners have to deal most of the time with (very) low sample sizes (think of small patient cohorts) along with very high dimensional data (think of neuroimaging data that are 3D volumes with millions of voxels). Unfortunately, this leads to a very poor representation of a given population and makes classical statistical analyses unreliable [1], [2]. Meanwhile, the remarkable performance of algorithms heavily relying on the deep learning framework [3] has made them extremely attractive and very popular. However, such results are strongly conditioned by the number of training samples since such models usually need to be trained on huge data sets to prevent over-fitting or to give statistically meaningful results [4].

A way to address such issues is to perform data augmentation (DA) [5]. In a nutshell, DA is the art of increasing the size of a given data set by creating synthetic labeled data. For instance, the easiest way to do this on images is to apply simple transformations such as the addition of Gaussian noise, cropping or padding, and assign the label of the initial image to the created ones. While such augmentation techniques have revealed very useful, they remain strongly data dependent and limited. Some transformations may indeed be uninformative or even induce bias. For instance, think of a digit representing a *6* which gives a *9* when rotated. While assessing the relevance of augmented data may be quite straightforward for simple data sets, it reveals very challenging for complex data and may require the intervention of an *expert* assessing the degree of relevance of the proposed transformations. In addition to the lack of data, imbalanced data sets also severely limit generalizability since they tend to bias the algorithm toward the most represented classes. Oversampling is a method that aims at balancing the number of samples per class by up-sampling the minority classes. The Synthetic Minority Over-sampling TEchnique (SMOTE) was first introduced in [6] and consists in interpolating data points belonging to the minority classes in their feature space. This approach was further extended in other works where the authors proposed to over-sample close to the decision boundary using either the k-Nearest Neighbor (k-NN) algorithm [7] or a support vector machine (SVM) [8] and so insist on samples that are potentially misclassified. Other over-sampling methods aiming at increasing the number of samples from the minority classes and taking into account their difficulty to be learned were also proposed [9], [10]. However, these

Data used in preparation of this article were obtained from the Alzheimer's Disease Neuroimaging Initiative (ADNI) database (http://adni.loni.usc.edu). As such, the investigators within the ADNI contributed to the design and implementation of ADNI and/or provided data but did not participate in analysis or writing of this report. A complete listing of ADNI investigators can be found at: http://adni.loni.usc.edu/wp-content/uploads/how_to_apply/ADNI_Acknowledgement_List.pdf

Data used in the preparation of this article was obtained from the Australian Imaging Biomarkers and Lifestyle flagship study of ageing (AIBL) funded by the Commonwealth Scientific and Industrial Research Organisation (CSIRO) which was made available at the ADNI database (http://adni.loni.usc.edu). The AIBL researchers contributed data but did not participate in analysis or writing of this report. AIBL researchers are listed at www.aibl.csiro.au.

- *Clément Chadebec and Stéphanie Allassonnière are with the Université de Paris, Inria, Centre de Recherche des Cordeliers, Inserm, Sorbonne Université, Paris, France*
- *Elina Thibeau-Sutre and Ninon Burgos are with Sorbonne Université, Institut du Cerveau - Paris Brain Institute (ICM), Inserm U 1127, CNRS UMR 7225, AP-HP Hôpital de la Pitié Salpêtrière and Inria Aramis project-team, Paris, France*

methods hardly scale to high-dimensional data [11], [12].

The recent rise in performance of generative models such as generative adversarial networks (GAN) [13] or variational autoencoders (VAE) [14], [15] has made them very attractive models to perform DA. GANs have already seen a wide use in many fields of application [16], [17], [18], [19], [20], including medicine [21]. For instance, GANs were used on magnetic resonance images (MRI) [22], [23], computed tomography (CT) [24], [25], X-ray [26], [27], [28], positron emission tomography (PET) [29], mass spectroscopy data [30], dermoscopy [31] or mammography [32], [33] and demonstrated promising results. Nonetheless, most of these studies involved either a quite large training set (above 1000 training samples) or quite small dimensional data, whereas in everyday medical applications it remains very challenging to gather such large cohorts of labeled patients. As a consequence, as of today, the case of high dimensional data combined with a very low sample size remains poorly explored. When compared to GANs, VAEs have only seen a very marginal interest to perform DA and were mostly used for speech applications [34], [35], [36]. Some attempts to use such generative models on medical data either for classification [37], [38] or segmentation tasks [39], [40], [41] can nonetheless be noted. The main limitation to a wider use of these models is that they most of the time produce blurry and fuzzy samples. This undesirable effect is even more emphasized when they are trained with a small number of samples which makes them very hard to use in practice to perform DA in the high dimensional (very) low sample size (HDLSS) setting.

In this paper, we argue that VAEs can actually be used for data augmentation in a reliable way even in the context of HDLSS data, provided that we bring some modeling of the latent space and amend the way we generate the data. Hence, in this paper we propose the following contributions:

- We propose to combine a proper modeling of the latent space of the VAE, here seen as a Riemannian manifold, and a new *geometry-aware non-prior*-based generation procedure which consists in sampling from the inverse of the Riemannian metric volume element. The choice of such a framework is discussed, motivated and compared to some other VAE models.
- We propose to use such a framework to perform data augmentation in the challenging context of HDLSS data. The robustness of the augmentation method to data sets and classifiers changes along with its reliance to the number of training samples is then tested through a series of experiments.
- We validate the proposed method on several *real-life* classification tasks on complex 3D MRI from ADNI and AIBL databases where the augmentation method allows for a significant gain in classification metrics even when only 50 samples per class are considered.

2 Variational Autoencoder

In this section, we quickly recall the idea behind VAEs along with some proposed improvements relevant to this paper.

2.1 Model Setting

Let $x \in \mathcal{X}$ be a set of data. A VAE aims at maximizing the likelihood of a given parametric model $\{\mathbb{P}_\theta, \theta \in \Theta\}$. It is assumed that there exist latent variables z living in a lower dimensional space $\mathcal{Z}$, referred to as the *latent space*, such that the marginal distribution of the data can be written as:

$$p_\theta(x) = \int_{\mathcal{Z}} p_\theta(x|z)q(z)dz\,, \tag{1}$$

where q is a prior distribution over the latent variables acting as a regulation factor and $p_\theta(x|z)$ is most of the time taken as a simple parametrized distribution (*e.g.* Gaussian, Bernoulli, etc.). Such a distribution is referred to as the *decoder*, the parameters of which are usually given by neural networks. Since the integral of Eq. (1) is most of the time intractable, so is the posterior distribution:

$$p_\theta(z|x) = \frac{p_\theta(x|z)q(z)}{\int_{\mathcal{Z}} p_\theta(x|z)q(z)dz}\,.$$

This makes direct application of Bayesian inference impossible and so recourse to approximation techniques such as variational inference [42] is needed. Hence, a variational distribution $q_\phi(z|x)$ is introduced and aims at approximating the true posterior distribution $p_\theta(z|x)$ [14]. This variational distribution is often referred to as the *encoder*. In the initial version of the VAE, q_ϕ is taken as a multivariate Gaussian whose parameters μ_ϕ and Σ_ϕ are again given by neural networks. Importance sampling can then be applied to derive an unbiased estimate of the marginal distribution $p_\theta(x)$ we want to maximize in Eq. (1)

$$\hat{p}_\theta(x) = \frac{p_\theta(x|z)q(z)}{q_\phi(z|x)} \quad \text{and} \quad \mathbb{E}_{z\sim q_\phi}\big[\hat{p}_\theta\big] = p_\theta(x)\,.$$

Using Jensen's inequality allows finding a lower bound on the objective function of Eq. (1)

$$\begin{aligned}\log p_\theta(x) &= \log \mathbb{E}_{z\sim q_\phi}\big[\hat{p}_\theta\big] \\ &\geq \mathbb{E}_{z\sim q_\phi}\big[\log \hat{p}_\theta\big] \\ &\geq \mathbb{E}_{z\sim q_\phi}\big[\log p_\theta(x,z) - \log q_\phi(z|x)\big] = ELBO\,.\end{aligned} \tag{2}$$

The Evidence Lower BOund (ELBO) is now tractable since both $p_\theta(x,z)$ and $q_\phi(z|x)$ are known and so can be optimized with respect to the *encoder* and *decoder* parameters.

2.2 Improving the Model: Literature Review

In recent years, many attempts to improve the VAE model have been made and we briefly discuss three main areas of improvement that are relevant to this paper in this section.

2.2.1 Enhancing the Variational Approximate Distribution

When looking at Eq. (2), it can be noticed that we are nonetheless trying to optimize only a lower bound on the true objective function. Therefore, much efforts have been focused on making this lower bound tighter and tighter [43], [44], [45], [46], [47], [48]. One way to do this is to enhance the expressiveness of the approximate posterior distribution q_ϕ. This is indeed due to the ELBO expression which can be also written as follows:

$$ELBO = \log p_\theta(x) - KL(q_\phi(z|x)||p_\theta(z|x))\,.$$

This expression makes two terms appear. The first one is the function we want to maximize while the second one is the Kullback–Leibler (KL) divergence between the approximate posterior distribution $q_\phi(z|x)$ and the true posterior $p_\theta(z|x)$. This very term is always non-negative and equals 0 if and only if $q_\phi = p_\theta$ almost everywhere. Hence, trying to tweak the approximate posterior distribution so that it becomes *closer* to the true posterior should make the ELBO tighter and enhance the model. To do so, a method proposed in [49] consisted in adding K Markov chain Monte Carlo (MCMC) sampling steps on the top of the approximate posterior distribution and targeting the true posterior. More precisely, the idea was to start from $z_0 \sim q_\phi(z|x)$ and use parametrized *forward* (resp. *reverse*) kernels $r(z_{k+1}|z_k, x)$ (resp. $r(z_k|z_{k+1}, x)$) to create a new estimate of the true marginal distribution $p_\theta(x)$. With the same objective, parametrized invertible mappings f_x called *normalizing flows* were instead proposed in [50] to *sample* z. A starting random variable z_0 is drawn from an initial distribution $q_\phi(z|x)$ and then K normalizing flows are applied to z_0 resulting in a random variable $z_K = f_x^K \circ \cdots \circ f_x^1(z_0)$ whose density writes:

$$q_\phi(z_K|x) = q_\phi(z_0|x) \prod_{k=1}^{K} |\det \mathbf{J}_{f_x^k}|^{-1},$$

where $\mathbf{J}_{f_x^k}$ is the Jacobian of the k^{th} normalizing flow. Ideally, we would like to have access to normalizing flows targeting the true posterior and allowing enriching the above distribution and so improve the lower bound. In that particular respect, a model inspired by the Hamiltonian Monte Carlo sampler [51] and relying on Hamiltonian dynamics was proposed in [49] and [52]. The strength of such a model relies in the choice of the normalizing flows which are guided by the gradient of the true posterior distribution.

2.2.2 Improving the Prior Distribution

While enhancing the approximate posterior distribution resulted in major improvements of the model, it was also argued that the prior distribution over the latent variables plays a crucial role as well [53]. Since the vanilla VAE uses a standard Gaussian distribution as prior, a natural improvement consisted in using a mixture of Gaussians instead [54], [55] which was further enhanced with the proposal of the variational mixture of posterior (VAMP) [56]. In addition, other models trying to change the prior distribution and relying on hierarchical latent variables have been proposed [43], [57], [58]. Prior learning is also a promising idea that has emerged (*e.g.* [59]) or more recently [60], [61], [62] and allows accessing complex prior distributions. Another approach relying on accept/reject sampling to improve the expressiveness of the prior distribution [63] can also be cited. While these proposals indeed improved the VAE model, the choice of the prior distribution remains tricky and strongly conditioned by the training data and the tractability of the ELBO.

2.2.3 Adding Geometrical Consideration to the Model

In the mean time, several papers have been arguing that geometrical aspects should also be taken into account. For instance, on the ground that the vanilla VAE fails to apprehend data having a latent space with a specific geometry, several latent space modelings were proposed as a hypershere [64] where Von-Mises distributions are considered instead of Gaussians or as a Poincare disk [65], [66]. Other works trying to introduce Riemannian geometry within the VAE framework proposed to model either the input data space [67], [68] or the latent space (or both) [69], [70], [71], [72] as Riemannian manifolds. The authors of [73] went further and bridged the gap with Sec. 2.2.1 by combining MCMC sampling and Riemannian metric learning within the model. They indeed proposed to see the latent space as a Riemannian manifold and instead learn a parametrized Riemannian metric over this space. This idea of Riemannian metric learning is attractive since it allows modeling the latent space as desired and was recently re-used and combined with prior learning [74].

3 The Proposed Method

In this section, we present the proposed method which consists in combining a proper latent space modeling with a new *non-prior* based generation scheme. We argue that while the vast majority of works dealing with VAE generate new data using the prior distribution, which is standard procedure, this is often sub-optimal, in particular in the context of small data sets. We indeed believe that the choice of the prior distribution is strongly data set dependent and is also constrained to be simple so that the ELBO in Eq. (2) remains tractable. Hence, the view adopted here is to consider the VAE only as a dimensionality reduction tool which is able to extract the latent structure of the data, *i.e.* the latent space modeled as the Riemannian manifold $(\mathbb{R}^d, g)$ where d is the dimension of the manifold and g is the associated Riemannian metric. Since the latent structure is *a-priori* far from being trivial, we propose in this paper to rely on the setting first introduced in [73] where the Riemannian metric is directly learned from the data. Before going further we first recall some elements on Riemannian geometry.

3.1 Some Elements on Riemannian Geometry

In the framework of differential geometry, one may define a Riemannian manifold $\mathcal{M}$ as a smooth manifold endowed with a Riemannian metric g that is a smooth inner product $g : p \to \langle \cdot|\cdot \rangle_p$ on the tangent space $T_p\mathcal{M}$ defined at each point of the manifold $p \in \mathcal{M}$. We call a chart (or coordinate chart) (U, φ) a homeomorphism mapping an open set U of the manifold to an open set V of an Euclidean space. The manifold is called a $d-$dimension manifold if for each chart of an atlas we further have $V \subset \mathbb{R}^d$. That is there exists a neighborhood U of each point p of the manifold such that U is homeomorphic to $\mathbb{R}^d$. Given $p \in U$, the chart $\varphi : (x^1, \ldots, x^d)$ induces a basis $\left(\frac{\partial}{\partial x^1}, \ldots, \frac{\partial}{\partial x^d}\right)_p$ on the tangent space $T_p\mathcal{M}$. Hence, a local representation of the metric of a Riemannian manifold in the chart (U, φ) can be written as a positive definite matrix $\mathbf{G}(p) = (g_{i,j})_{p, 0 \leq i,j \leq d} = (\langle \frac{\partial}{\partial x^i} | \frac{\partial}{\partial x^j} \rangle_p)_{0 \leq i,j \leq d}$ at each point $p \in U$. That is for $v, w \in T_p\mathcal{M}$ and $p \in U$, we have $\langle u|w \rangle_p = u^\top \mathbf{G}(p) w$. Since we propose to work in the ambient-like manifold $(\mathbb{R}^d, g)$, there exists a global chart

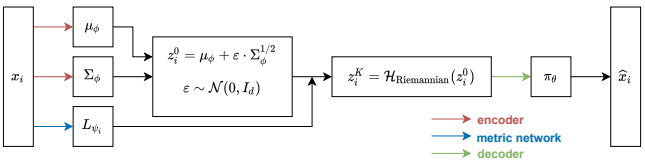

Fig. 1. Geometry-aware VAE framework. Neural networks are highlighted with the colored arrows and $\mathcal{H}_{\text{Riemannian}}$ are the normalizing flows using Riemannian Hamiltonian equations. π_θ represents the parameters of the decoder (*e.g.* Gaussian, Bernoulli, etc.).

given by $\varphi = id$. Hence, for the following, we assume that we work in this coordinate system and so $\mathbf{G}$ will refer to the metric's matrix representation in this chart.

There are two ways to apprehend manifolds. The extrinsic view assumes that the manifold is embedded within a higher dimensional Euclidean space (think of the 2-dimensional sphere $\mathcal{S}^2$ embedded within $\mathbb{R}^3$). The intrinsic view, which is adopted in this paper, does not make such an assumption since the manifold is studied using its underlying structure. For example, a curve's length cannot be interpreted using the distance defined on an Euclidean space but requires the use of the metric defined onto the manifold itself. The length of a curve γ between two points of the manifold $z_1, z_2 \in \mathcal{M}$ and parametrized by $t \in [0, 1]$ such that $\gamma(0) = z_1$ and $\gamma(1) = z_2$ is then given by

$$\mathcal{L}(\gamma) = \int_0^1 \|\dot{\gamma}(t)\|_{\gamma(t)} \mathrm{d}t = \int_0^1 \sqrt{\langle \dot{\gamma}(t) | \dot{\gamma}(t) \rangle_{\gamma(t)}} \mathrm{d}t \,.$$

Curves minimizing such a length are called *geodesics* and a distance dist between elements of a (connected) manifold can be introduced as follows:

$$\mathrm{dist}(z_1, z_2) = \inf_\gamma \mathcal{L}(\gamma) \quad \text{s.t.} \quad \gamma(0) = z_1, \gamma(1) = z_2 \quad (3)$$

The manifold $\mathcal{M}$ is said to be *geodesically complete* if all geodesic curves can be extended to $\mathbb{R}$. In other words, at each point p of the manifold one may draw a *straight* line (with respect to the formerly defined distance) indefinitely and in any direction.

3.2 Setting

Since the latent space is here seen as the Riemannian manifold $(\mathbb{R}^d, g)$, it is in particular characterised by the Riemannian metric g whose choice is very important. While several attempts have been made to try to put a Riemannian structure over the latent space of VAEs [70], [71], [72], [75], [76], [77], the proposed metrics involved the Jacobian of the generator function which is hard to use in practice and is constrained by the generator network architecture. As a consequence, we instead decide to rely on the idea of Riemannian metric learning [78].

3.2.1 The Metric

As discussed before, the Riemannian metric plays a crucial role in the modeling of the latent space. In this paper, we decide to use a parametric metric inspired from [79] having the following matrix representation:

$$\mathbf{G}^{-1}(z) = \sum_{i=1}^{N} L_{\psi_i} L_{\psi_i}^\top \exp\Big(- \frac{\|z - c_i\|_2^2}{T^2} \Big) + \lambda I_d \,, \quad (4)$$

where N is the number of observations, L_{ψ_i} are lower triangular matrices with positive diagonal coefficients learned from the data and parametrized with neural networks, c_i are referred to as the *centroids* and correspond to the mean $\mu_\phi(x_i)$ of the encoded distributions of the latent variables z_i ($z_i \sim q_\phi(z_i|x_i) = \mathcal{N}(\mu_\phi(x_i), \Sigma_\phi(x_i))$, T is a temperature scaling the metric close to the *centroids* and λ is a regularization factor that also scales the metric tensor far from the latent codes. The shape of this metric is very powerful since we have access to a closed-form expression of the inverse metric tensor which is usually useful to compute shortest paths (through the exponential map). Moreover, this metric is very smooth, differentiable everywhere and allows scaling the Riemannian volume element $\sqrt{\det \mathbf{G}(z)}$ far from the data very easily through the regularization factor λ. A similar metric was proposed in [69] but was used in the input data space $\mathcal{X}$ and is not learned from the data. To be able to refer to geodesics on the entire learned manifold we need the following proposition (proved in Appendix A. in the supplementary materials).

Proposition 1. The Riemannian manifold $(\mathbb{R}^d, g)$ is *geodesically complete*.

3.2.2 The Model

The metric is learned in the same way as proposed in [73] since we rely on Riemannian Hamiltonian dynamics [80], [81]. The main idea is to encode the input data points x_i and so get the means $\mu_\phi(x_i)$ of the posterior distributions associated with the encoded latent variables $z_i^0 \sim \mathcal{N}(\mu_\phi(x_i), \Sigma_\phi(x_i))$. These means are then used to update the metric centroids c_i. In the mean time, the input data points x_i are fed to another neural network which outputs the matrices L_{ψ_i} used to update the metric. The updated metric is then used to *sample* z_i^K from the z_i^0 the same way it is done with normalizing flows [50] but Riemannian Hamiltonian equations are employed instead. The z_i^K are then fed to the decoder network which outputs the parameters of the conditional distribution $p_\theta(x|z)$. The reparametrization trick is used to sample z_i^0 as is common and since the Riemannian Hamiltonian equations are *deterministic*, back-propagation can be performed to update all the parameters. A scheme of the *geometry-aware* VAE model framework can be found in Fig. 1. In the following, we will refer to the proposed model either as *geometry-aware VAE* or *RHVAE* for short. An implementation using PyTorch [82] is available in the supplementary materials.

3.2.3 Sampling from the Latent Space

In this paper, we propose to amend the standard sampling procedure of classic VAEs to better exploit the Riemannian structure of the latent space. The *geometry-aware* VAE is here seen as a tool able to capture the intrinsic latent structure of the data and so we propose to exploit this property directly within the generation procedure. This differs greatly from the standard fully probabilistic view where the prior distribution is used to generate new data. We believe that such an approach remains far from being optimal when one considers small data sets since, depending on its choice, the prior may either poorly prospect the latent space or sample in locations without any usable information. This

is discussed and illustrated in Sec. 3.2.4 and Sec. 3.3. We instead propose to sample from the following distribution:

$$p(z) = \frac{\rho_S(z)\sqrt{\det \mathbf{G}^{-1}(z)}}{\int\limits_{\mathbb{R}} \rho_S(z)\sqrt{\det \mathbf{G}^{-1}(z)dz}}\,, \tag{5}$$

where S is a compact set[1] so that the integral is well defined. Fortunately, since we use a parametrized metric given by Eq. (4) and whose inverse has a closed form, it is pretty straightforward to evaluate the numerator of Eq. (5). Then, classic MCMC sampling methods can be employed to sample from p on $\mathbb{R}^d$. In this paper, we propose to use the Hamiltonian Monte Carlo (HMC) sampler [83] since the gradient of the log-density is computable. Given a target density p_{target} we want to sample from, the idea behind the HMC sampler is to introduce a random variable $v \sim \mathcal{N}(0, I_d)$ independent from z and rely on Hamiltonian dynamics. Analogous to physical systems, z may be seen as the *position* and v as the *velocity* of a particle whose potential energy $U(z)$ and kinetic energy $K(v)$ are given by

$$U(z) = -\log p_{\text{target}}(z), \qquad K(v) = \frac{1}{2}v^\top v\,.$$

These two energies give together the Hamiltonian [84], [85]

$$H(z, v) = U(z) + K(v)\,.$$

The evolution in time of such a particle is governed by Hamilton's equations as follows

$$\frac{\partial z_i}{\partial t} = \frac{\partial H}{\partial v_i}, \qquad \frac{\partial v_i}{\partial t} = -\frac{\partial H}{\partial z_i}\,.$$

Such equations can be integrated using a discretization scheme known as the *Stormer-Verlet* or *leapfrog* integrator which is run l times

$$\begin{aligned} v(t+\varepsilon/2) &= v(t) - \frac{\varepsilon}{2}\cdot \nabla_z U(z(t))\,,\\ z(t+\varepsilon) &= z(t) + \varepsilon \cdot v(t+\varepsilon/2)\,,\\ v(t+\varepsilon) &= v(t+\varepsilon/2) - \frac{\varepsilon}{2}\nabla_z U(z(t+\varepsilon))\,, \end{aligned} \tag{6}$$

where ε is the integrator step size. The HMC sampler produces a Markov chain (z^n) with the aforementioned integrator. More precisely, given z_0^n, the current state of the chain, an initial *velocity* is sampled $v_0 \sim \mathcal{N}(0, I_d)$ and then Eq. (6) are run l times to move from $(z_0^n,\, v_0)$ to $(z_l^n,\, v_l)$. The proposal z_l^n is then accepted with probability $\alpha = \min\left(1, \frac{\exp(-H(z_l^n, v_l))}{\exp(-H(z_0^n, v_0))}\right)$. It was shown that the chain (z^n) is time-reversible and converges to its stationary distribution p_{target} [51], [84], [86].

In our method p_{target} is given by Eq. (4) and Eq. (5). Fortunately, since the HMC sampler allows sampling from densities known up to a normalizing constant (thanks to the acceptance ratio), the computation of the denominator of p_{target} is not needed and the Hamiltonian follows

$$H(z, v) = U(z) + K(v) \propto -\frac{1}{2}\log\det \mathbf{G}^{-1}(z) + \frac{1}{2}v^\top v$$

and is easy to compute. Hence, the only *difficulty* left is the computation of the gradient $\nabla_z U(z)$ needed in the *leapfrog* integrator which is actually pretty straightforward using the chain rule. In this paper, a typical choice for ε and l, the sampler's parameters, is $\varepsilon \in [0.01, 0.05]$ and $l \in [10, 15]$. We would also like to mention the recent work of [77] where the authors used the distribution $q(z) \propto (1 + \sqrt{\det \mathbf{G}(z)})^{-1}$ to sample from a Wasserstein GAN [87]. Nonetheless, both the framework and the metric remain quite different.

1. Take for instance $\{z \in \mathcal{Z}, \|z\| \leq 2 \cdot \max_i \|c_i\|\}$

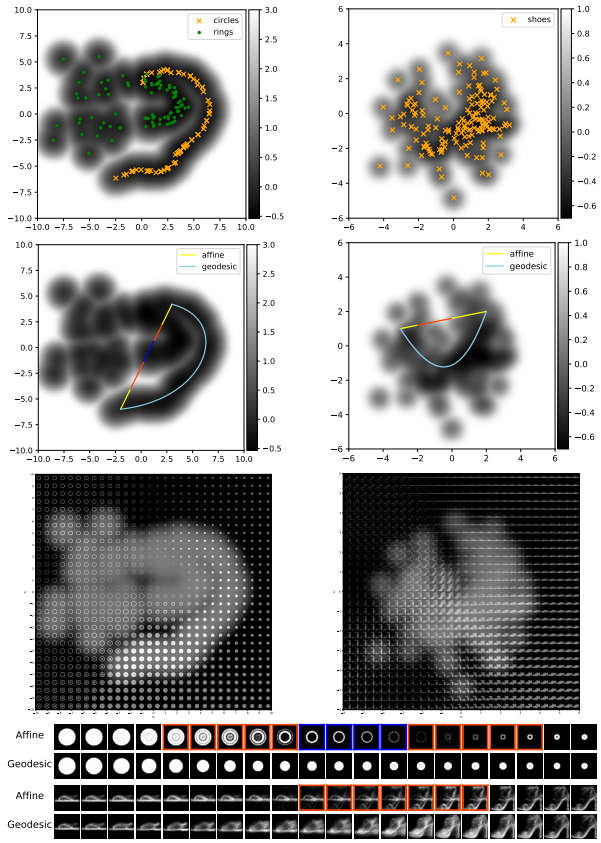

Fig. 2. Geodesic interpolations under the learned metric in two different latent spaces. Top: Latent spaces with the log metric volume element presented in gray scale. Second row: The resulting interpolations under the Euclidean metric or the Riemannian metric. Third row: The learned manifolds and corresponding decoded samples. Bottom: Decoded samples all along the interpolation curves.

3.2.4 *Discussion on the Sampling Distribution*

One may wonder what is the rationale behind the use of the distribution p formerly defined in Eq. (5). By design, the metric is such that the metric volume element $\sqrt{\det \mathbf{G}(z)}$ is scaled by the factor λ far from the encoded data points. Hence, choosing a relatively small λ imposes that shortest paths travel through the most populated area of the latent space, *i.e.* next to the latent codes. As such, the metric volume element can be seen as a way to quantify the amount of information contained at a specific location of the latent space. The smaller the volume element the more information we have access to. Fig. 2 illustrates well these aspects. On the first row are presented two learned latent spaces along with the log of the metric volume element displayed in gray scale for two different data sets. The first one is composed of 180 binary circles and rings of different diameters and thicknesses while the second one is composed of 160 samples extracted from the FashionMNIST data set [88].

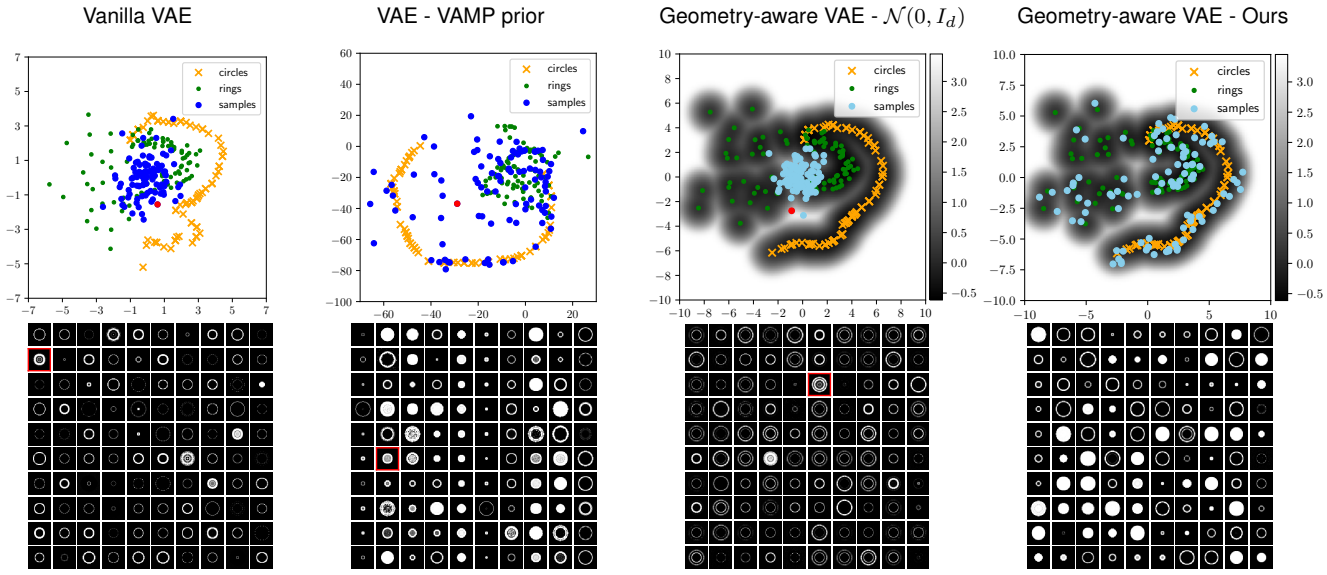

Fig. 3. VAE sampling comparison. Top: The learned latent space along with the means $\mu_\phi(x_i)$ of the latent code distributions (colored dots and crosses) and 100 latent space samples (blue dots) using either the prior distribution or the proposed scheme. For the *geometry-aware* VAEs, the log metric volume element is presented in gray scale in the background. Bottom: The 100 corresponding decoded samples in the data space.

The means $\mu_\phi(x_i)$ of the distributions associated with the latent variables are presented with the crosses and dots for each class. As expected, the metric volume element is smaller close to the latent variables since small λ's were considered (10^{-3} resp. 10^{-1}). A common way to study the learned Riemannian manifold consists in finding geodesic curves, *i.e.* the shortest paths with respect to the learned Riemannian metric. Hence, on the second row of Fig. 2, we compare two types of interpolation in each latent space. For each experiment, we pick two points in the latent space and perform either a linear or a geodesic interpolation (*i.e.* using the Riemannian metric). The bottom row illustrates the decoded samples all along each interpolation curve while the third one displays the decoded samples according to the latent space location of the corresponding codes. The first outcome of such an experiment is that, as expected, geodesic curves travel next to the codes and so do not explore areas of the latent space with no information whereas linear interpolations do. Therefore, decoding along geodesic curves produces far better and more meaningful interpolations in the input data space since in both cases we clearly see the starting sample being progressively distorted until the path reaches the ending point. This allows for instance interpolating between two shoes and keep the intrinsic topology of the data all along the path since each decoded sample on the interpolation curve looks like a shoe. This is made impossible under the Euclidean metric where shortest paths are straight lines and so may travel through areas of least interest. For instance, the affine interpolation travels through areas with no latent data and so produces decoded samples that are mainly a superposition of samples (see the red lines and corresponding decoded samples framed in red) or crosses areas with codes belonging to the other class (see the blue line and the corresponding blue frames). This point is even more supported by the plots in the third row of Fig. 2 where we clearly see that locations with the highest metric volume element are often less relevant. This study demonstrates that most of the information in the latent space is contained next to the codes and so, if we want to generate new samples that look-like the input data, we need to sample next to them and that is why we elected the distribution of Eq. (5).

3.3 Generation Comparison

In this section, we propose to compare the new generation procedure with other *prior-based* methods in the context of low sample size data sets.

3.3.1 Qualitative Comparison

First, we validate the proposed generation method on a hand-made synthetic data set composed of 180 binary circles and rings of different diameters and thicknesses (see Appendix C). We then train 1) a vanilla VAE, 2) a VAE with VAMP prior [56], 3) a *geometry-aware* VAE but using the prior to generate and 4) a *geometry-aware* VAE with the proposed generation scheme, and compare the generated samples. Each model is trained until the ELBO does not improve for 20 epochs and any relevant parameter setting is made available in Appendix B. In Fig. 3, we compare the sampling obtained with the vanilla VAE (left column), the VAE with VAMP prior (2^{nd} column), the *geometry-aware* VAE using a standard normal distribution as prior (3^{rd} column) and the *geometry-aware* VAE using the proposed sampling method (*i.e.* sampling from the inverse of the metric volume element). The first row presents the learned latent spaces along with the means of the encoded training data points for each class (crosses and dots) and 100 samples issued by the generation methods (blue dots). For the RHVAE models, the log metric volume element $\sqrt{\det \mathbf{G}}$ is also displayed in gray scale in the background. The bottom row shows the resulting 100 decoded samples in the data space.

TABLE 1
GAN-train (the higher the better) and *GAN-test* (the closer to the baseline the better) scores. A benchmark DenseNet model is trained with five independent runs on the generated data $\mathcal{S}_g$ (resp. the *real* train set $\mathcal{S}_{\text{train}}$) and tested on the *real* test set $\mathcal{S}_{\text{test}}$ (resp. $\mathcal{S}_g$) to compute the *GAN-train* (resp. *GAN-test*) score. 1000 synthetic samples per class are considered for $\mathcal{S}_g$ so that it matches the size of $\mathcal{S}_{\text{test}}$.

	reduced MNIST (balanced)		*reduced* MNIST (unbalanced)		*reduced* EMNIST	
Metric	GAN-train	GAN-test	GAN-train	GAN-test	GAN-train	GAN-test
Baseline	90.6 ± 1.2	-	82.8 ± 0.7	-	84.5 ± 1.3	-
VAE - $\mathcal{N}(0, I_d)$	83.4 ± 2.4	67.1 ± 4.9	74.7 ± 3.2	52.8 ± 10.6	75.3 ± 1.4	54.5 ± 6.5
VAMP	84.1 ± 3.0	74.9 ± 4.3	28.5 ± 8.9	61.4 ± 7.0	43.2 ± 4.4	58.1 ± 7.7
RHVAE - $\mathcal{N}(0, I_d)$	82.0 ± 2.9	63.1 ± 4.1	69.3 ± 1.8	46.9 ± 8.4	73.6 ± 4.1	55.6 ± 5.0
Ours	$\mathbf{90.1 \pm 1.4}$	$\mathbf{88.1 \pm 2.7}$	$\mathbf{86.2 \pm 1.8}$	$\mathbf{83.8 \pm 4.0}$	$\mathbf{82.6 \pm 1.3}$	$\mathbf{76.0 \pm 4.0}$

The first outcome of this experiment is that sampling from the prior distribution leads to a quite poor latent space prospecting. This drawback is very well illustrated when a standard Gaussian distribution is used to sample from the latent space (see 1^{st} and 3^{rd} column of the 1^{st} row). The prior distribution having a higher mass close to zero will insist on latent samples close to the origin. Unfortunately, in such a case, latent codes close to the origin only belong to a single class (rings). Therefore, even though the number of training samples was roughly the same for circles and rings, we end up with a model over-generating samples belonging to a certain class (rings) and even to a specific type of data within this very class. This undesirable effect seems even ten-folded when considering the *geometry-based* VAE model since adding MCMC steps in the training process, as explained in Fig. 1, tends to stretch the latent space. It can be nonetheless noted that using a multi-modal prior such as the VAMP prior mitigates this and allows for a better prospecting. However, such a model remains hard to fit when trained with small data sets [56]. Another limitation of prior-based generation methods relies in their inability to assess a given sample quality. They may indeed sample in areas of the latent space containing very little information and so conduct to generated samples that are meaningless. This appears even more striking when small data sets are considered. An interesting observation that was noted among others in [75] is that neural networks tend to interpolate very poorly in *unseen* locations (i.e. far from the training data points). When looking at the *decoded* latent samples (bottom row of Fig. 3) we eventually end up with the same conclusion. Actually, it appears that the networks interpolate quite linearly between the training data points in our case. This may be illustrated for instance by the red dots in the latent spaces in Fig. 3 whose corresponding decoded sample is framed in red. The sample is located *between* two classes and when decoded it produces an image mainly corresponding to a superposition of samples belonging to different classes. This aspect is also supported by the observations made when discussing the relevance of geodesic interpolations on Fig. 2 of Sec. 3.2.4. Therefore, these drawbacks may conduct to a (very) poor representation of the actual data set diversity while presenting quite a few *irrelevant* samples. Obviously the notion of *irrelevance* is here disputable but if the objective is to represent a given set of data we expect the generated samples to be close to the training data while having some specificities to enrich it. Impressively, sampling against the inverse of the metric volume element as proposed in Sec. 3.2.3 allows for a far more meaningful sample generation. Furthermore, the new sampling scheme avoids regions with no latent code, which thus contain poor information, and focuses on areas of interest so that almost every decoded sample is visually satisfying. Similar effects are observed on *reduced* EMNIST [89], *reduced* MNIST [90] and *reduced* FashionMNIST data sets and higher dimensional latent spaces (dimension 10) where samples are most of the time degraded when the classic generation is employed while the new one allows the generation of more diverse and sharper samples (see Appendix C). Finally, the proposed method does not overfit the training data since the samples are not always located on the centroids, and the quantitative metrics of the following section also support this point.

3.3.2 Quantitative Comparison

In order to compare quantitatively the diversity and relevance of the samples generated by a generative model, several measures have been proposed [91], [92], [93], [94]. Since those metrics suffer from some drawbacks [95], [96], we decide to use the *GAN-train* / *GAN-test* measure discussed in [95] as it appears to us well suited to measure the ability of a generative model to perform data augmentation. These two metrics consist in comparing the accuracy of a benchmark classifier trained on a set of generated data $\mathcal{S}_g$ and tested on a set of *real* images $\mathcal{S}_{\text{test}}$ (*GAN-train*) or trained on the original train set $\mathcal{S}_{\text{train}}$ (*real* images used to train the generative model) and tested on $\mathcal{S}_g$ (*GAN-test*). Those accuracies are then compared to the baseline accuracy given by the same classifier trained on $\mathcal{S}_{\text{train}}$ and tested on $\mathcal{S}_{\text{test}}$. These two metrics are quite interesting for our application since the first one (*GAN-train*) measures the quality and diversity of the generated samples (the higher the better) while the second one (*GAN-test*) accounts for the generative model's tendency to overfit (a score significantly higher than the baseline accuracy means overfitting). Ideally, the closer to the baseline the *GAN-test* score is the better. To stick to our low sample size setting, we compute these scores on three data sets created by down-sampling well-known databases. The first data set is created by extracting 500 samples from 10 classes of MNIST ensuring balanced classes. For the second one, 500 samples of the MNIST database are again considered but a random split is applied such that some classes are under-represented. The last one consists in selecting 500 samples from 10 classes of the EMNIST data set having both lowercase and uppercase

letters. These three data sets are then divided into a baseline train set $\mathcal{S}_{\text{train}}$ (80%) and a validation set $\mathcal{S}_{\text{val}}$ (20%) used for the classifier training. Since the initial databases are huge, we use the original test set for $\mathcal{S}_{\text{test}}$ so that it provides statistically meaningful results. The same generative models as in Sec. 3.3.1 are then trained on each class of $\mathcal{S}_{\text{train}}$ to generate 1000 samples per class and $\mathcal{S}_g$ is created for each VAE by gathering all generated samples. A benchmark classifier chosen as a DenseNet [97] is then 1) trained on $\mathcal{S}_{\text{train}}$ and tested on $\mathcal{S}_{\text{test}}$ (*baseline*); 2) trained on $\mathcal{S}_g$ and tested on $\mathcal{S}_{\text{test}}$ (*GAN-train*) and 3) trained on $\mathcal{S}_{\text{train}}$ and tested on $\mathcal{S}_g$ (*GAN-test*) until the loss does not improve for 50 epochs on $\mathcal{S}_{\text{val}}$. For each experiment, the model is trained five times and we report the mean score and the associated standard deviation in Table 1. As expected, the proposed method allows producing samples that are far more meaningful and relevant, in particular to perform DA. This is first illustrated by the *GAN-train* scores that are either very close to the accuracy obtained with the *baseline* or higher (see MNIST (unbalanced) in Table 1). The fact that we are able to enhance the classifier's accuracy even when trained only with synthetic data is very encouraging. Firstly, it proves that the created samples are close to the *real* ones and so that we were able to capture the true distribution of the data. Secondly, it shows that we do not overfit the initial training data since we are able to add some relevant information through the synthetic samples. This last observation is also supported by the *GAN-test* scores for the proposed method which are quite close to the accuracies achieved on the *baseline*. In case of overfitting, the *GAN-test* score is expected to be significantly higher than the baseline since the classifier is tested on the generated samples while trained on the *real* data that were also used to train the generative model. Having a score close to the baseline illustrates that the generative model is able to capture the distribution of the data and does not only *memorize* it [95].

4 Data Augmentation: Evaluation and Robustness

In this section we show the relevance of the proposed improvements to perform data augmentation in a HDLSS setting through a series of experiments.

4.1 Setting

The setting we employ for data augmentation consists in selecting a data set and splitting it into a train set (the *baseline*), a validation set and a test set. The *baseline* is then augmented using the proposed VAE framework and generation procedure. The generated samples are finally added to the original train set (*i.e.* the *baseline*) and fed to a classifier. The whole data augmentation procedure is illustrated in Fig. 4 for a convolutional neural network (CNN) model as classifier.

4.2 Toy Data Sets

The proposed VAE framework is here used to perform DA on several down-sampled well-known databases such that only tens of *real* training samples per class are considered so that we stick to the low sample size setting. First, the robustness of the method across these data sets is tested with a standard benchmark classifier. Then, the method's reliability across other common classifiers is stressed. Finally, its scalability to larger data sets is discussed.

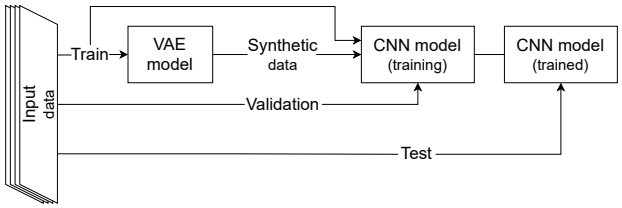

Fig. 4. Overview of the data augmentation procedure. The input data set is divided into a train set (the *baseline*), a validation set and a test set. The train set is augmented using the VAE framework and generated data are then added to the *baseline* to train a benchmark classifier.

4.2.1 Materials

The first data set is created by selecting 500 samples from the ten classes of the MNIST data set ensuring balanced classes. We will refer to it as *reduced* MNIST. The second one consists in selecting again 500 samples from the MNIST database but applying a random split such that some classes are over-represented. We call it the *reduced unbalanced* MNIST data set. Then, we create another one using the FashionMNIST data set and three classes we find hard to distinguish (*i.e. T-shirt*, *dress* and *shirt*). The data set is composed of 300 samples ensuring balanced classes and is referred to as *reduced* Fashion. Finally, we also select 500 samples from ten classes of the EMNIST. These classes are selected such that they are composed of both lowercase and uppercase characters so that we end up with a small database with strong variability within classes. The balance matches the one in the initial data set (*by merge*). In summary, we built four data sets having different class numbers, class splits and sample sizes. These data sets are then divided such that 80% is allocated for training (referred to as the *Baseline*) and 20% for validation. Since the original data sets are huge, we decide to use the test set provided in the original databases (*e.g.* ≈1000 samples per class for MNIST and Fashion) such that it provides statistically meaningful results while allowing for a reliable assessment of the model's generalization power on unseen data.

4.2.2 Robustness Across Data Sets

The first experiment we conduct consists in assessing the method's robustness across the four aforementioned data sets. For this study, we propose to consider a DenseNet [97] model[2] as benchmark classifier. On the one hand, the training data (the *baseline*) is augmented by a factor 5, 10 and 15 using classic data augmentation methods (random noise, random crop, rotation, etc.) so that the proposed method can be compared with classic and simple augmentation techniques. On the other hand, the protocol described in Fig. 4 is employed with a vanilla VAE and a *geometry-aware* VAE. The generative models are trained individually on each class of the *baseline* until the ELBO does not improve for 20 epochs. The VAEs are then used to produce 200, 500,

2. We used the PyTorch implementation provided in [98]

TABLE 2
Data augmentation with a DenseNet model as benchmark. Mean accuracy and standard deviation across five independent runs are reported. The first three rows (Aug.) correspond to basic transformations (noise, crop, etc.). In gray are the cells where the accuracy is higher on synthetic data than on the *baseline* (*i.e.* the raw data). The test set is the one proposed in the entire original data set (*e.g.* ≈1000 samples per class for MNIST) so that it provides statistically meaningful results and allows for a good assessment of the model's generalization power.

	MNIST	MNIST (unbal.)	EMNIST (unbal.)	FASHION
Baseline	89.9 ± 0.6	81.5 ± 0.7	82.6 ± 1.4	76.0 ± 1.5
Baseline + Synthetic				
Aug. (X5)	92.8 ± 0.4	86.5 ± 0.9	85.6 ± 1.3	77.5 ± 2.0
Aug. (X10)	88.2 ± 2.2	82.0 ± 2.4	85.7 ± 0.3	79.2 ± 0.6
Aug. (X15)	92.8 ± 0.7	85.8 ± 3.4	86.6 ± 0.8	80.0 ± 0.5
VAE-200*	88.5 ± 0.9	84.0 ± 2.0	81.7 ± 3.0	78.6 ± 0.4
VAE-500*	90.4 ± 1.3	87.3 ± 1.2	83.4 ± 1.6	78.7 ± 0.3
VAE-1k*	91.2 ± 1.0	86.0 ± 2.5	84.3 ± 1.6	77.6 ± 2.1
VAE-2k*	92.2 ± 1.6	88.0 ± 2.2	86.0 ± 0.2	79.3 ± 1.1
RHVAE-200*	89.9 ± 0.5	82.3 ± 0.9	83.0 ± 1.3	77.6 ± 1.3
RHVAE-500*	90.9 ± 1.1	84.0 ± 3.2	84.4 ± 1.2	78.0 ± 1.3
RHVAE-1k*	91.7 ± 0.8	84.7 ± 1.8	84.7 ± 2.4	79.3 ± 1.6
RHVAE-2k*	92.7 ± 1.4	86.8 ± 1.0	84.9 ± 2.1	79.0 ± 1.4
Ours-200	91.0 ± 1.0	84.1 ± 2.0	85.1 ± 1.1	77.0 ± 0.8
Ours-500	92.3 ± 1.1	87.7 ± 0.9	85.1 ± 1.1	78.5 ± 0.9
Ours-1k	93.2 ± 0.8	$\mathbf{89.7 \pm 0.8}$	87.0 ± 1.0	$\mathbf{80.2 \pm 0.8}$
Ours-2k	$\mathbf{94.3 \pm 0.8}$	89.1 ± 1.9	$\mathbf{87.6 \pm 0.8}$	78.1 ± 1.8
Synthetic Only				
VAE-200*	69.9 ± 1.5	64.6 ± 1.8	65.7 ± 2.6	73.9 ± 3.0
VAE-500*	72.3 ± 4.2	69.4 ± 4.1	67.3 ± 2.4	71.4 ± 8.5
VAE-1k*	83.4 ± 2.4	74.7 ± 3.2	75.3 ± 1.4	71.4 ± 6.1
VAE-2k*	86.5 ± 2.2	79.6 ± 3.8	78.8 ± 3.0	76.7 ± 1.6
RHVAE-200*	76.0 ± 1.8	61.5 ± 2.9	59.8 ± 2.6	72.8 ± 3.6
RHVAE-500*	80.0 ± 2.2	66.8 ± 3.3	66.9 ± 4.0	74.3 ± 2.6
RHVAE-1k*	82.0 ± 2.9	69.3 ± 1.8	73.6 ± 4.1	76.0 ± 4.1
RHVAE-2k*	85.2 ± 3.9	77.3 ± 3.2	68.6 ± 2.3	74.3 ± 3.1
Ours-200	87.2 ± 1.1	79.5 ± 1.6	77.0 ± 1.6	77.0 ± 0.8
Ours-500	89.1 ± 1.3	80.4 ± 2.1	80.2 ± 2.0	78.5 ± 0.8
Ours-1k	90.1 ± 1.4	86.2 ± 1.8	82.6 ± 1.3	79.3 ± 0.6
Ours-2k	92.6 ± 1.1	87.5 ± 1.3	86.0 ± 1.0	78.3 ± 0.9

* Using a standard normal prior to generate

1000 and 2000 new synthetic samples per class using either the classic generation scheme (*i.e.* sampling with the prior $\mathcal{N}(0, I_d)$) or the proposed generation procedure referred to as *ours*. Finally, the benchmark DenseNet model is trained with five independent runs on either 1) the *baseline*, 2) the augmented data using classic augmentation methods, 3) the augmented data using the VAEs or 4) only the synthetic data created by the generative models. For each experiment, the mean accuracy and the associated standard deviation across those five runs is reported in Table 2. An early stopping strategy is employed and CNN training is stopped if the loss does not improve on the validation set for 50 epochs.

The first outcome of such a study is that, as expected, generating synthetic samples with the proposed method seems to enhance their relevance when compared with other models, in particular for data augmentation tasks. This is for instance illustrated by the second section of Table. 2 where synthetic samples are added to the *baseline*. While adding samples generated either by the VAE or RHVAE and using the prior distribution seems to improve the classifier accuracy when compared with the *baseline*, the gain remains limited since it struggles to exceed the gain reached with classic augmentation methods. For instance, neither the VAE nor the RHVAE allows the classifier to achieve a better score on *reduced* MNIST or *reduced* EMNIST data sets. On the contrary, the proposed generation method is able to produce very useful samples for the CNN model. Adding the generated data to the *baseline* indeed allows for a great gain in the model accuracy which exceeds the one achieved with any other method while keeping a relatively low standard deviation on each data set (highlighted in bold).

Secondly, the relevance of the samples produced by the proposed scheme is even more supported by the last section of Table 2 where the classifier is trained only using the synthetic samples generated by the VAEs. First, even with a quite small number of generated samples (200 per class), the classifier is almost able to reach the accuracy achieved on the *baseline*. For instance, when the CNN is trained on *reduced* MNIST with 200 synthetic samples per class generated with our method, it is able to achieve an accuracy of 87.2% vs. 89.9% with the *baseline*. In comparison, both the VAE and RHVAE fail to produce meaningful samples when the prior is used since a loss of 15 to 20 points in accuracy is observed, combined with a potentially very strong loss in confidence making those samples *unreliable*. The fact that the classifier almost performs as well on the synthetic data as on the *baseline* is good news since it shows that the proposed framework is able to produce samples accounting for the original data set diversity even with a small number of generated samples. Even more interesting, as the number of synthetic data increases, the classifier is able to perform much better on the synthetic data than on the *baseline* since a gain of 3 to 6 points in accuracy is observed. Again, this strengthens the observations made in Sec. 3.3.1 and Sec. 3.3.2 where it was noted that **the proposed method is able to enrich the initial data set** with relevant and realistic samples.

Finally, it can be seen in this experiment why geometric data augmentation methods are still questionable and remain data set dependent. For example, augmenting the *baseline* by a factor 10 (where we add flips and rotations on the original data) seems to have no significant effect on the *reduced* MNIST data sets while it still improves results on *reduced* EMNIST and FashionMNIST. We see here how the *expert* knowledge comes into play to assess the relevance of the transformations applied to the data. Fortunately, the method we propose does not require such knowledge and **appears to be quite robust to data set changes.**

4.2.3 Robustness Across Classifiers

In addition to assessing the robustness of the method to data sets changes, we also propose to evaluate its reliability across classifiers. To do so, we consider very different common supervised classifiers: a multi layer perceptron (MLP) [3], a random forest [99], the k-NN algorithm and a SVM [100]. Each of the aforementioned classifiers is again trained either on 1) the original training data set (the *baseline*); 2) the augmented data using the proposed method and 3) only the synthetic data generated by our method with five independent runs and using the same data sets as presented in Sec. 4.2.1. Finally, we report the mean accuracy and standard deviation across these runs for each classifier and data set. The results for the balanced (resp. unbalanced) *reduced* MNIST data set can be found in Fig. 5a (resp. Fig. 5b). Metrics obtained on the two other data sets are available in Appendix D but reflect the same tendency.

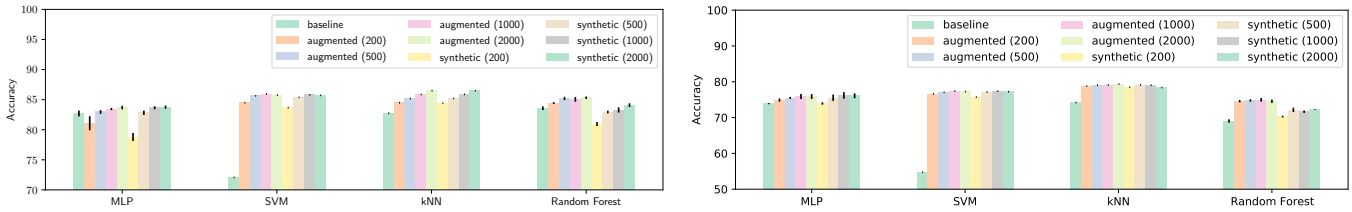

(a) *reduced* MNIST balanced

(b) *reduced* MNIST unbalanced

Fig. 5. Evolution of the accuracy of four benchmark classifiers on *reduced* balanced MNIST (left) and *reduced* unbalanced MNIST data sets (right). Stochastic classifiers are trained with five independent runs and we report the mean accuracy and standard deviation on the test set.

As illustrated in Fig. 5, the method appears quite robust to classifier changes as well since it allows improving the model's accuracy significantly for almost all classifiers (the accuracy achieved on the *baseline* is presented by the leftmost bar in Fig. 5 for each classifier). The method's strength is even more striking when unbalanced data sets are considered since the method is able to produce meaningful samples even with a very small number of training data and so it is able to over-sample the minority classes in a reliable way. Moreover, as observed in the previous sections, synthetic samples are again helpful to enhance classifiers' generalization power since they perform better when trained only on synthetic data than on the *baseline* in almost all cases.

4.2.4 A Note on the Method Scalability

Finally, we also quickly discuss the method scalability to larger data sets. To do so, we consider the MNIST data set and a benchmark classifier taken as a DenseNet which performs well on such data. Then, we down-sample the original MNIST database in order to progressively decrease the number of samples per class. We start by creating a data set having 1000 samples per class to finally reach 20 samples per class. For each created data set, we allocate 80% for training (the *baseline*) and reserve 20% for the validation set. A *geometry-aware* VAE is then trained on each class of the *baseline* until the ELBO does not improve for 50 epochs and is used to generate synthetic samples (12.5× the *baseline*). The benchmark CNN is trained with five independent runs on either 1) the *baseline*, 2) the augmented data or 3) only the synthetic data generated with our model. The evolution of the mean accuracy on the original test set (≈1000 samples per class) according to the number of samples per class is presented in Fig. 6. The first outcome of this experiment is that the fewer samples in the training set, the more useful the method appears. Using the proposed augmentation framework indeed allows for a gain of more than 9.0 points in the CNN accuracy when only 20 samples per class are considered. In other words, as the number of samples increases, the marginal gain seems to decrease. Nevertheless, this reduction must be put into perspective since it is commonly acknowledged that, as the results on the *baseline* increase (and thus get closer to the perfect score), it is even more challenging to improve the score with the augmented data. In this experiment, we are nonetheless still able to improve the model accuracy even when it already achieves a very high score. For instance, with 500 samples per class, the augmentation method still allows increasing

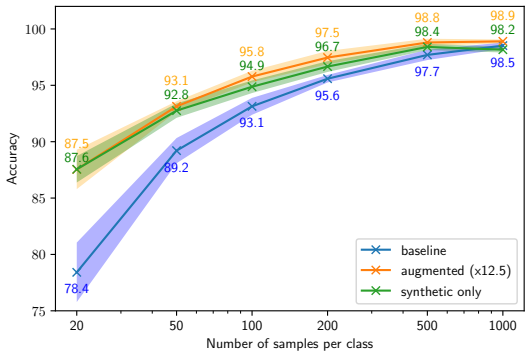

Fig. 6. Evolution of the accuracy of a benchmark CNN classifier according to the number of samples per class in the train set (*i.e.* the *baseline*) on MNIST. The VAE is trained on each class of the *baseline* to augment its size by a factor 12.5. A CNN is then trained 5 times on 1) the *baseline* (blue), 2) the augmented *baseline* (orange) and 3) only the synthetic data (green). The curves show the mean accuracy and associated standard deviation on the original test set.

the model accuracy from 97.7% to 98.8%. Finally, for data sets with fewer than 500 samples per class, the classifier is again able to outperform the *baseline* even when trained only with the synthetic data. This shows again the strong generalization power of the proposed method which allows creating new relevant data for the classifier.

5 Validation on Medical Imaging

With this last series of experiments, we assess the validity of our data augmentation framework on a binary classification task consisting in differentiating Alzheimer's disease (AD) patients from cognitively normal (CN) subjects based on T1-weighted (T1w) MR images of human brains. Such a task is performed using a CNN trained, as before, either on 1) *real* images, 2) synthetic samples or 3) both. In this section, label definition, preprocessing, quality check, data split and CNN training and evaluation is done using Clinica[3] and ClinicaDL[4], two open-source software packages for neuroimaging processing.

5.1 Data Augmentation Literature for AD vs CN Task

Even though many studies use CNNs to differentiate AD from CN subjects with anatomical MRI [101], we did not

3. https://github.com/aramis-lab/clinica
4. https://github.com/aramis-lab/AD-DL

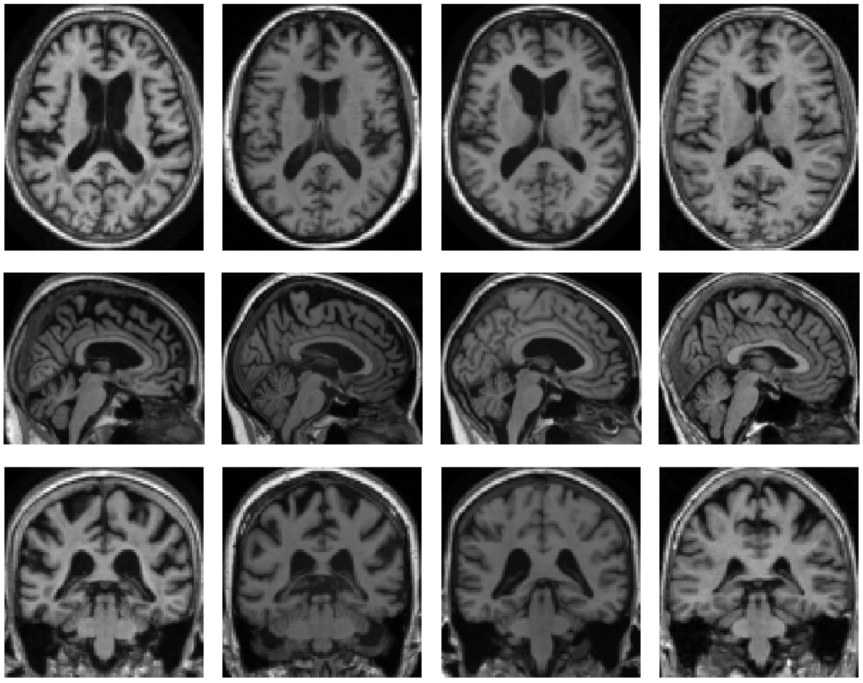

Fig. 7. Example of two *true* patients compared to two generated by our method. Can you find the intruders ? Answers in Appendix F

find any meta-analysis on the use of data augmentation for this task. Some results involving DA can nonetheless be cited and are presented in Table 4. However, assessing the real impact of data augmentation on the performance of the model remains challenging. For instance, this is illustrated by the works of [102] and [103], which are two examples in which DA was used and led to two significantly different results, although a similar framework was used in both studies. Interestingly, as shown in Table 4, studies using DA for this task only relied on simple affine and pixel-level transformations, which may reveal data dependent. Note that complex DA was actually performed for AD vs CN classification tasks on PET images, but PET is less frequent than MRI in neuroimaging data sets [104]. As noted in the previous sections, our method would apply pretty straightforwardly to this modality as well. For MRI, other techniques such as transfer learning [105] and weak supervision [106] were preferred to handle the small amount of samples in data sets and may be coupled with DA to further improve the network performance.

TABLE 3
Summary of participant demographics, mini-mental state examination (MMSE) and global clinical dementia rating (CDR) scores at baseline.

Data set	Label	Obs.	Age	Sex M/F	MMSE	CDR
ADNI	CN	403	73.3 ± 6.0	185/218	29.1 ± 1.1	0: 403
	AD	362	74.9 ± 7.9	202/160	23.1 ± 2.1	0.5: 169, 1: 192 2: 1
AIBL	CN	429	73.0 ± 6.2	183/246	28.8 ± 1.2	0: 406, 0.5: 22 1: 1
	AD	76	74.4 ± 8.0	33/43	20.6 ± 5.5	0.5: 31, 1: 36 2: 7, 3: 2

5.2 Materials

Data used in this section are obtained from the Alzheimer's Disease Neuroimaging Initiative (ADNI) database (adni.loni.usc.edu) and the Australian Imaging, Biomarkers and Lifestyle (AIBL) study (aibl.csiro.au).

The ADNI was launched in 2003 as a public-private partnership, led by Principal Investigator Michael W. Weiner, MD. The primary goal of ADNI has been to test whether serial MRI, PET, other biological markers, and clinical and neuropsychological assessment can be combined to measure the progression of mild cognitive impairment and early AD. For up-to-date information, see www.adni-info.org. The ADNI data set is composed of four cohorts: ADNI-1, ADNI-GO, ADNI-2 and ADNI-3. The data collection of ADNI-3 has not ended yet, hence our data set contains all images and metadata that were already available on May 6, 2019. Similarly to ADNI, the AIBL data set seeks to discover which biomarkers, cognitive characteristics, and health and lifestyle factors determine the development of AD. This cohort is also longitudinal and the diagnosis is given according to a series of clinical tests [110]. Data collection for this cohort is over.

Two diagnoses are considered for the classification task:

- CN: baseline session of participants who were diagnosed as cognitively normal at baseline and stayed stable during the follow-up;
- AD: baseline session of participants who were diagnosed as demented at baseline and stayed stable during the follow-up.

Table 3 summarizes the demographics, the mini-mental state examination (MMSE) and global clinical dementia rating (CDR) scores at baseline of the participants included in our data set. The MMSE and the CDR scores are classical

TABLE 4
Accuracy obtained by studies performing AD vs CN classification with CNNs applied on T1w MRI and using data augmentation

				Accuracy	
Study	Methods	Participants	Images	Baseline	Augmented
Valliani and Soni, 2017 [107]	rotation, flip, shift	417	417	78.8	81.3
Backstrom et al., 2018 [108]	flip	340	1198	–	90.1
Cheng and Liu, 2017 [109]	shift, sampling, rotation	193	193	–	85.5
Aderghal et al., 2017 [102]	shift, blur, flip	720	720	82.8	83.7
Aderghal et al., 2018 [103]	shift, blur	720	720	–	90.0

clinical scores used to assess dementia. The MMSE score has a maximal value of 30 for cognitively normal persons and decreases if symptoms are detected. The CDR score has a minimal value of 0 for cognitively normal persons and increases if symptoms are detected.

5.3 Preprocessing of T1-Weighted MRI

The steps performed in this section correspond to the procedure followed in [101] and are listed below:

1) Raw data are converted to the BIDS standard [111],
2) Bias field correction is applied using N4ITK [112],
3) T1w images are linearly registered to the MNI standard space [113], [114] with ANTS [115] and cropped. This produced images of size $169\times208\times179$ with 1 mm^3 isotropic voxels.
4) An automatic quality check is performed using an open-source pretrained network [116]. All images passed the quality check.
5) NIfTI files are converted to tensor format.
6) (Optional) Images are down-sampled using a trilinear interpolation, leading to an image size of $84\times104\times89$.
7) Intensity rescaling between the minimum and maximum values of each image is performed.

These steps lead to 1) down-sampled images ($84\times104\times89$) or 2) high-resolution images ($169\times208\times179$).

5.4 Evaluation Procedure

The ADNI data set is split into three sets: training, validation and test. First, the test set is created using 100 randomly chosen participants for each diagnostic label (i.e. 100 CN, 100 AD). The rest of the data set is split between the training (80%) and the validation (20%) sets. We ensure that age, sex and site distributions between the three sets are not significantly different.

A smaller training set (denoted as *train-50*) is extracted from the obtained training set (denoted as *train-full*). This set comprises only 50 images per diagnostic label, instead of 243 CN and 210 AD for *train-full*. We ensure that age and sex distributions between *train-50* and *train-full* are not significantly different. This is not done for the site distribution as there are more than 50 sites in the ADNI data set (so they could not all be represented in this smaller training set). AIBL data are never used for training or hyperparameter tuning and are only used as an independent test set.

5.5 CNN Classifiers

A CNN takes as input an image and outputs a vector of size C corresponding to the number of labels existing in the data set. Then, the prediction of the CNN for a given image corresponds to the class with the highest probability in the output vector.

5.5.1 Hyperparameter Choices

As for the VAE, the architecture of the CNN depends on the size of the input. Then there is one architecture per input size: down-sampled images and high-resolution images (see Fig. 8). Moreover, two different paradigms are used to choose the architecture. First, we reuse the same architecture as in [101]. This architecture is obtained by optimizing manually the networks on the ADNI data set for the same task (AD vs CN). A slight adaption is done for the down-sampled images, which consists in resizing the number of nodes in the fully-connected layers to keep the same ratio between the input and output feature maps in all layers. We denote these architectures as **baseline**. Secondly, we launch a random search [117] that allows exploring different hyperperameter values. The hyperparameters explored for the architecture are the number of convolutional blocks, of filters in the first layer and of convolutional layers in a block, the number of fully-connected layers and the dropout rate. Other hyperparameters such as the learning rate and the weight decay are also part of the search. 100 different random architectures are trained on the 5-fold cross-validation done on *train-full*. For each input, we choose the architecture that obtained the best mean balanced accuracy across the validation sets of the cross-validation. We denote these architectures as **optimized**.

5.5.2 Network Training

The weights of the convolutional and fully-connected layers are initialized as described in [118], which corresponds to the default initialization method in PyTorch. Networks are trained for 100 epochs for **baseline** and 50 epochs for **optimized**. The training and validation losses are computed with the cross-entropy loss. For each experiment, the final model is the one that obtained the highest validation balanced accuracy during training. The balanced accuracy of the model is evaluated at the end of each epoch.

5.6 Experimental Protocol

As done in the previous sections, we perform three types of experiments and train the model on 1) only the *real* images, 2) only on synthetic data and 3) on synthetic and real images. Due to the current implementation, augmentation on

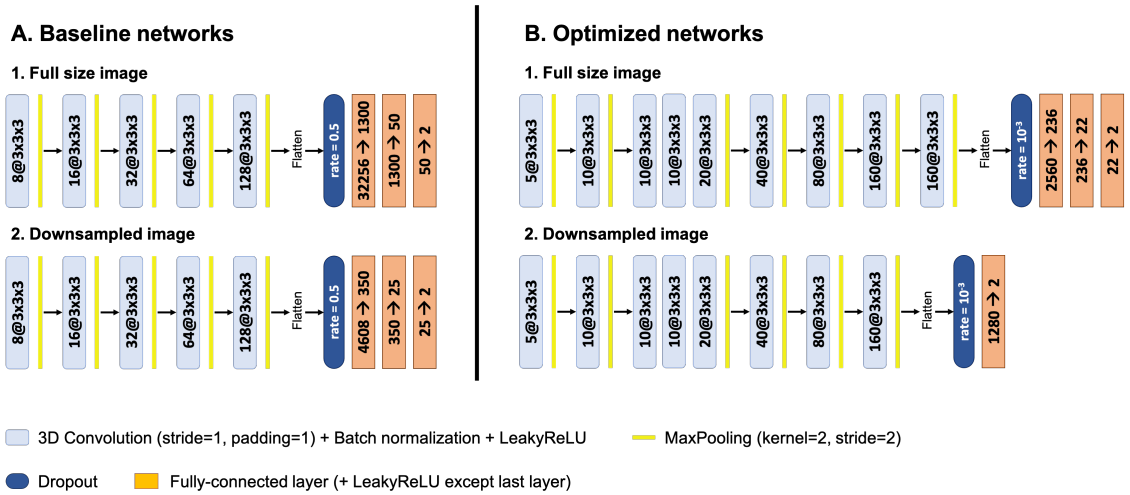

Fig. 8. Diagrams of the network architectures used for classification. The first **baseline** architecture (A1) is the one used in [101], the second one (A2) is a very similar one adapted to process smaller inputs. The **optimized** architectures (B1) and (B2) are obtained independently with two different random searches. For convolution layers we specify the number of channels @ the kernel size and for the fully-connected layers we specify the number of input nodes → the number of output nodes. Each fully-connected layer is followed by a LeakyReLU activation except for the last one. For the dropout layer, the dropout rate is specified.

high-resolution images is not possible and so these images are only used to assess the baseline performance of the CNN with the maximum information available. Each series of experiments is done once for each training set (*train-50* and *train-full*). The CNN and the VAE share the same training set, and the VAE does not use the validation set during its training. For each training set, two VAEs are trained, one on the AD label only and the other on the CN label only. Examples of real and generated AD images are shown in Fig. 7. For each experiment 20 runs of the CNN training are launched. The use of a smaller training set *train-50* allows mimicking the behavior of the framework on smaller data sets, which are frequent in the medical domain.

5.7 Results

Results presented in Table 5 (resp. Table 6) are obtained with **baseline** (resp. **optimized**) hyperparameters and using either the *train-full* or *train-50* data set. Scores on synthetic images only are given in Appendix G. Experiments are done on down-sampled images unless *high-resolution* is specified.

Even though the VAE augmentation is performed on down-sampled images, the classification performance is at least as good as that of the best baseline performance, or can greatly exceed it:

- on *train-50* with **baseline** hyperparameters the increase of balanced accuracy is of 6.2 points on ADNI and 8.9 points on AIBL,
- on *train-full* with **baseline** hyperparameters the increase of balanced accuracy is of 5.7 points on ADNI and 4.7 on AIBL,
- on *train-50* with **optimized** hyperparameters the increase of balanced accuracy is of 2.5 points on ADNI and 6.3 points on AIBL,
- on *train-full* with **optimized** hyperparameters the increase of balanced accuracy is of 1.5 point on ADNI and -0.1 point on AIBL,

Then, the performance increase thanks to DA is higher when using the **baseline** hyperparameters than the **optimized** ones. A possible explanation could be that the **optimized** network is already close to the maximum performance that can be reached with this setup and cannot be much improved with DA. Moreover, the hyperparameters of the VAE have not been subject to a similar search, so this places it at a disadvantage. For both hyperparameters, the performance gain is higher on *train-50* than on *train-full*, which supports the results obtained in the previous section (see Fig. 6).

The baseline balanced accuracy with the **baseline** hyperparameters on *train-full*, 80.6% on ADNI and 80.4% on AIBL, are similar to the results of [101]. With DA, we improve our balanced accuracy to 86.3% on ADNI and 85.1% on AIBL: this performance is similar to their result using autoencoder pretraining (which can be very long to compute) and longitudinal data (1830 CN and 1106 AD images) instead of baseline data (243 CN and 210 AD images) as we did.

In each table, the first two rows display the baseline performance obtained on real images only. As expected, training on high-resolution images leads to a better performance than training on down-sampled images. This is not the case for the **optimized** network on *train-50*, which obtained a balanced accuracy of 72.1% on ADNI and 71.2% on AIBL with high-resolution images versus 75.5% on ADNI and 75.6% on AIBL with down-sampled images. This is explained by the fact that the hyperparameters choice is made on *train-full* and so there is no guarantee that it could lead to similar results with fewer data samples.

6 Discussion

Contrary to techniques that are specific to a field of application, our method produced relevant data for diverse data sets including 2D natural images (MNIST, EMNIST and FASHION) or 3D medical images (ADNI and AIBL). Moreover, we note that the networks learning on medical

TABLE 5
Mean test performance of each series of 20 runs trained with the **baseline** hyperparameters

training set	data set	ADNI sensitivity	ADNI specificity	ADNI balanced accuracy	AIBL sensitivity	AIBL specificity	AIBL balanced accuracy
train-50	real	70.3 ± 12.2	62.4 ± 11.5	66.3 ± 2.4	60.7 ± 13.7	73.8 ± 7.2	67.2 ± 4.1
	real (high-resolution)	78.5 ± 9.4	57.4 ± 8.8	67.9 ± 2.3	57.2 ± 11.2	75.8 ± 7.0	66.5 ± 3.0
	500 synthetic + real	71.9 ± 5.3	67.0 ± 4.5	69.4 ± 1.6	55.9 ± 6.8	81.1 ± 3.1	68.5 ± 2.5
	1000 synthetic + real	69.8 ± 6.6	71.2 ± 3.7	70.5 ± 2.1	59.1 ± 9.0	82.1 ± 3.7	70.6 ± 3.1
	2000 synthetic + real	72.2 ± 4.4	70.3 ± 4.3	71.2 ± 1.6	66.6 ± 7.1	79.0 ± 4.1	72.8 ± 2.2
	3000 synthetic + real	71.8 ± 4.9	73.4 ± 5.5	72.6 ± 1.6	66.1 ± 9.3	81.1 ± 5.0	73.6 ± 3.0
	5000 synthetic + real	$\mathbf{74.7 \pm 5.3}$	$\mathbf{73.5 \pm 4.8}$	$\mathbf{74.1 \pm 2.2}$	$\mathbf{71.7 \pm 10.0}$	80.5 ± 4.4	$\mathbf{76.1 \pm 3.6}$
	10000 synthetic + real	74.7 ± 7.0	73.4 ± 6.1	74.0 ± 2.7	69.1 ± 9.9	$\mathbf{80.7 \pm 5.1}$	74.9 ± 3.2
train-full	real	79.1 ± 6.2	76.3 ± 4.2	77.7 ± 2.5	70.6 ± 6.7	86.3 ± 3.6	78.4 ± 2.4
	real (high-resolution)	84.5 ± 3.8	76.7 ± 4.0	80.6 ± 1.1	71.6 ± 6.4	89.2 ± 2.7	80.4 ± 2.6
	500 synthetic + real	82.5 ± 3.4	81.9 ± 5.4	82.2 ± 2.4	76.0 ± 6.3	89.7 ± 3.3	82.9 ± 2.5
	1000 synthetic + real	84.6 ± 4.4	84.3 ± 5.1	84.4 ± 1.8	77.0 ± 7.0	90.4 ± 3.4	83.7 ± 2.3
	2000 synthetic + real	$\mathbf{85.4 \pm 4.0}$	86.4 ± 5.9	85.9 ± 1.6	77.2 ± 6.9	90.4 ± 3.8	83.8 ± 2.2
	3000 synthetic + real	84.7 ± 3.6	86.8 ± 4.5	85.8 ± 1.7	77.2 ± 4.8	$\mathbf{91.7 \pm 2.9}$	84.4 ± 1.8
	5000 synthetic + real	84.6 ± 4.2	86.9 ± 3.6	85.7 ± 2.1	76.9 ± 5.2	91.4 ± 3.0	84.2 ± 2.2
	10000 synthetic + real	84.2 ± 2.8	$\mathbf{88.5 \pm 2.9}$	$\mathbf{86.3 \pm 1.8}$	$\mathbf{79.1 \pm 4.7}$	91.0 ± 2.6	$\mathbf{85.1 \pm 1.9}$

TABLE 6
Mean test performance of each series of 20 runs trained with the **optimized** hyperparameters

training set	image type	ADNI sensitivity	ADNI specificity	ADNI balanced accuracy	AIBL sensitivity	AIBL specificity	AIBL balanced accuracy
train-50	real	75.4 ± 5.0	75.5 ± 5.3	75.5 ± 2.7	68.6 ± 8.5	82.6 ± 4.2	75.6 ± 4.1
	real (high-resolution)	73.6 ± 6.2	70.6 ± 5.9	72.1 ± 3.1	57.8 ± 12.3	84.6 ± 4.2	71.2 ± 5.1
	500 synthetic + real	73.2 ± 4.2	78.0 ± 3.3	75.6 ± 2.5	69.2 ± 9.4	$\mathbf{82.7 \pm 4.1}$	76.0 ± 4.2
	1000 synthetic + real	76.1 ± 5.3	$\mathbf{79.5 \pm 2.9}$	77.8 ± 2.3	79.3 ± 5.8	82.5 ± 4.2	80.9 ± 3.2
	2000 synthetic + real	75.2 ± 3.8	78.6 ± 4.4	76.9 ± 2.4	77.8 ± 8.8	82.2 ± 4.5	80.0 ± 3.6
	3000 synthetic + real	76.5 ± 3.8	79.2 ± 4.2	77.8 ± 1.9	80.9 ± 7.9	81.4 ± 4.2	81.2 ± 3.7
	5000 synthetic + real	77.1 ± 3.7	76.7 ± 4.1	76.9 ± 2.5	80.7 ± 6.1	81.2 ± 3.7	80.9 ± 2.7
	10000 synthetic + real	$\mathbf{77.8 \pm 4.6}$	78.2 ± 4.9	$\mathbf{78.0 \pm 2.1}$	$\mathbf{81.7 \pm 4.9}$	81.9 ± 4.6	$\mathbf{81.9 \pm 2.2}$
train-full	real	82.5 ± 4.2	88.5 ± 6.6	85.5 ± 2.4	75.1 ± 8.4	88.7 ± 9.0	81.9 ± 3.2
	real (high-resolution)	82.6 ± 4.5	88.9 ± 6.3	85.7 ± 2.5	78.9 ± 5.4	89.9 ± 4.0	84.4 ± 1.7
	500 synthetic + real	82.3 ± 2.3	89.8 ± 2.7	86.0 ± 1.8	74.9 ± 5.0	91.4 ± 2.6	83.2 ± 2.4
	1000 synthetic + real	82.5 ± 3.3	90.5 ± 4.1	86.5 ± 1.9	76.4 ± 5.6	91.0 ± 3.4	83.7 ± 2.0
	2000 synthetic + real	$\mathbf{83.1 \pm 4.2}$	$\mathbf{91.3 \pm 3.2}$	$\mathbf{87.2 \pm 1.7}$	76.0 ± 4.7	92.0 ± 2.4	84.0 ± 2.0
	3000 synthetic + real	81.3 ± 3.7	90.4 ± 3.4	85.8 ± 2.6	74.9 ± 7.3	92.3 ± 2.6	83.6 ± 3.2
	5000 synthetic + real	81.9 ± 3.5	90.9 ± 2.5	86.4 ± 1.3	74.1 ± 4.9	$\mathbf{92.9 \pm 1.9}$	83.5 ± 2.2
	10000 synthetic + real	82.2 ± 3.4	91.2 ± 3.6	86.7 ± 1.8	$\mathbf{76.4 \pm 4.2}$	92.1 ± 2.1	$\mathbf{84.3 \pm 1.8}$

images of ADNI gave similar balanced accuracies on the ADNI test subset and AIBL. This shows that our synthetic data learned on ADNI benefit in the same way to AIBL, and that it did not overfit the characteristics of ADNI.

In addition to the robustness across data sets, the usability of synthetic data by diverse classifiers was assessed. For toy data sets these classifiers were a MLP, a random forest, k-NN algorithm and a SVM. On medical image data sets, two different CNN were studied: a **baseline** one that has been only slightly optimized in a previous study and an **optimized** one found with a more extensive search (random search). All these classifiers performed best on augmented data than real data only. However, we note that the data augmentation was more beneficial to the **baseline** network, than to the **optimized** one but both networks obtained a similar performance with data augmentation on the largest training set. This means that data augmentation could avoid spending time and/or resources optimizing a classifier.

The ability of the model to generate relevant data and enrich the original training data was also supported by the fact that almost all classifiers could achieve a better classification performance when trained only on synthetic data than on the *real* train set.

Our generation framework appears also very well suited to perform data augmentation in a HDLSS setting (the binary classification of AD and CN subjects using T1w MRI). In all cases the classification performance was at least as good as the maximum performance obtained with real data and could even be much better. For instance, the method allowed the balanced accuracy of the **baseline** CNN to jump from 66.3% to 74.3% when trained with only 50 images per class and from 77.7% to 86.3% when trained with 243 CN and 210 AD while still improving greatly sensitivity and specificity metrics. We witnessed a greater performance improvement than the other studies using a CNN on T1w MRI to differentiate AD and CN subjects [102], [103], [107],

[108], [109]. Indeed, these studies used simple transforms (affine and pixel-wise) that may not bring enough variability to improve the CNN performance. Though many complex methods now exist to perform data augmentation, they are still not widely adopted in the field of medical imaging. We suspect that this is mainly due to the lack of reproducibility of such frameworks. Hence we provide the source code, as well as scripts to easily reproduce the experiments of this paper from the ADNI and AIBL data set download to the final evaluation of the CNN performance.

Nonetheless, the performance of our classification on synthetic data could be improved in many ways. First, we chose in this study not to spend much time optimizing the hyperparameters of the VAE and hence in Sec. 5 we chose to work with down-sampled images to deal with memory issues more easily. We could look for another architecture to train the VAE directly on high-resolution images, leading to a better performance, as witnessed in experiments on real images only. Moreover, we could couple the advantages of other techniques such as autoencoder pretraining or weak supervision to our data augmentation framework. However, the advantages may not stack as observed when using data augmentation on optimized hyperparameters. Finally, we chose to train our networks with only one image per participant, but our framework could also benefit from the use of the whole follow-up of all patients to further improve performance. However, a long follow-up is rather an exception in the context of medical imaging. This is why we assessed the relevance of our data augmentation framework in the context of small data sets, which is a main issue in this field. Nonetheless, a training set of 50 images per class can still be seen as large in the case of rare diseases and so it may be interesting to evaluate the reliability of our method on even smaller training sets (20 or 10 images per class).

7 Conclusion

In this paper, we proposed a new VAE-based data augmentation framework whose performance and robustness were validated on classification tasks on *toy* and *real-life* data sets. This method relies on the combination of a proper latent space modeling of the VAE seen as a Riemannian manifold and a new generation procedure exploiting such geometrical aspects. In particular, the generation method does not use the prior as is standard since we showed that, depending on its choice and the data set considered, it may lead to a very poor latent space prospecting and a degraded sampling while the proposed method does not suffer from such drawbacks. The proposed amendments were motivated, discussed and compared to other VAE models and demonstrated promising results. The model indeed appeared to be able to generate new data faithfully and demonstrated a strong generalization power which makes it very well suited to perform data augmentation even in the challenging context of HDLSS data. For each augmentation experiment, it was able to enrich the initial data set so that a classifier performs better on augmented data than only on the *real* ones. Future work would consist in building a framework able to handle longitudinal data and so able to generate not only one observation but a whole patient trajectory.

Acknowledgment

The research leading to these results has received funding from the French government under management of Agence Nationale de la Recherche as part of the "Investissements d'avenir" program, reference ANR-19-P3IA-0001 (PRAIRIE 3IA Institute) and reference ANR-10-IAIHU-06 (Agence Nationale de la Recherche-10-IA Institut Hospitalo-Universitaire-6). This work was granted access to the HPC resources of IDRIS under the allocation 101637 made by GENCI (Grand Équipement National de Calcul Intensif).

Data collection and sharing for this project was funded by the Alzheimer's Disease Neuroimaging Initiative (ADNI) (National Institutes of Health Grant U01 AG024904) and DOD ADNI (Department of Defense award number W81XWH-12-2-0012). ADNI is funded by the National Institute on Aging, the National Institute of Biomedical Imaging and Bioengineering, and through generous contributions from the following: AbbVie, Alzheimer's Association; Alzheimer's Drug Discovery Foundation; Araclon Biotech; BioClinica, Inc.; Biogen; Bristol-Myers Squibb Company; CereSpir, Inc.; Cogstate; Eisai Inc.; Elan Pharmaceuticals, Inc.; Eli Lilly and Company; EuroImmun; F. Hoffmann-La Roche Ltd and its affiliated company Genentech, Inc.; Fujirebio; GE Healthcare; IXICO Ltd.; Janssen Alzheimer Immunotherapy Research & Development, LLC.; Johnson & Johnson Pharmaceutical Research & Development LLC.; Lumosity; Lundbeck; Merck & Co., Inc.; Meso Scale Diagnostics, LLC.; NeuroRx Research; Neurotrack Technologies; Novartis Pharmaceuticals Corporation; Pfizer Inc.; Piramal Imaging; Servier; Takeda Pharmaceutical Company; and Transition Therapeutics. The Canadian Institutes of Health Research is providing funds to support ADNI clinical sites in Canada. Private sector contributions are facilitated by the Foundation for the National Institutes of Health (www.fnih.org). The grantee organization is the Northern California Institute for Research and Education, and the study is coordinated by the Alzheimer's Therapeutic Research Institute at the University of Southern California. ADNI data are disseminated by the Laboratory for Neuro Imaging at the University of Southern California.

References

[1] K. S. Button, J. P. Ioannidis, C. Mokrysz, B. A. Nosek, J. Flint, E. S. Robinson, and M. R. Munafò, "Power failure: why small sample size undermines the reliability of neuroscience," *Nature Reviews Neuroscience*, vol. 14, no. 5, pp. 365–376, 2013.

[2] B. O. Turner, E. J. Paul, M. B. Miller, and A. K. Barbey, "Small sample sizes reduce the replicability of task-based fMRI studies," *Communications Biology*, vol. 1, no. 1, pp. 1–10, 2018.

[3] I. Goodfellow, Y. Bengio, A. Courville, and Y. Bengio, *Deep learning*. MIT press Cambridge, 2016, vol. 1, issue: 2.

[4] C. Shorten and T. M. Khoshgoftaar, "A survey on Image Data Augmentation for Deep Learning," *Journal of Big Data*, vol. 6, no. 1, p. 60, 2019.

[5] M. A. Tanner and W. H. Wong, "The calculation of posterior distributions by data augmentation," *Journal of the American statistical Association*, vol. 82, no. 398, pp. 528–540, 1987.

[6] N. V. Chawla, K. W. Bowyer, L. O. Hall, and W. P. Kegelmeyer, "SMOTE: synthetic minority over-sampling technique," *Journal of artificial intelligence research*, vol. 16, pp. 321–357, 2002.

[7] H. Han, W.-Y. Wang, and B.-H. Mao, "Borderline-SMOTE: A new over-sampling method in imbalanced data sets learning," in *Advances in Intelligent Computing*, D.-S. Huang, X.-P. Zhang, and G.-B. Huang, Eds. Springer Berlin Heidelberg, 2005, vol. 3644, pp. 878–887, series Title: LNCS.

[8] H. M. Nguyen, E. W. Cooper, and K. Kamei, "Borderline over-sampling for imbalanced data classification," *International Journal of Knowledge Engineering and Soft Data Paradigms*, vol. 3, no. 1, pp. 4–21, 2011.

[9] Haibo He, Yang Bai, E. A. Garcia, and Shutao Li, "ADASYN: Adaptive synthetic sampling approach for imbalanced learning," in *2008 IEEE International Joint Conference on Neural Networks (IEEE World Congress on Computational Intelligence)*. IEEE, 2008, pp. 1322–1328.

[10] S. Barua, M. M. Islam, X. Yao, and K. Murase, "MWMOTE–majority weighted minority oversampling technique for imbalanced data set learning," *IEEE Transactions on Knowledge and Data Engineering*, vol. 26, no. 2, pp. 405–425, 2012.

[11] R. Blagus and L. Lusa, "SMOTE for high-dimensional class-imbalanced data," *BMC Bioinformatics*, vol. 14, no. 1, p. 106, 2013.

[12] A. Fernández, S. Garcia, F. Herrera, and N. V. Chawla, "SMOTE for learning from imbalanced data: progress and challenges, marking the 15-year anniversary," *Journal of artificial intelligence research*, vol. 61, pp. 863–905, 2018.

[13] I. Goodfellow, J. Pouget-Abadie, M. Mirza, B. Xu, D. Warde-Farley, S. Ozair, A. Courville, and Y. Bengio, "Generative adversarial nets," in *Advances in Neural Information Processing Systems*, 2014, pp. 2672–2680.

[14] D. P. Kingma and M. Welling, "Auto-encoding variational bayes," *arXiv:1312.6114 [cs, stat]*, 2014.

[15] D. J. Rezende, S. Mohamed, and D. Wierstra, "Stochastic back-propagation and approximate inference in deep generative models," in *International conference on machine learning*. PMLR, 2014, pp. 1278–1286.

[16] X. Zhu, Y. Liu, J. Li, T. Wan, and Z. Qin, "Emotion classification with data augmentation using generative adversarial networks," in *Pacific-Asia conference on knowledge discovery and data mining*. Springer, 2018, pp. 349–360.

[17] G. Mariani, F. Scheidegger, R. Istrate, C. Bekas, and C. Malossi, "BAGAN: Data Augmentation with Balancing GAN," *arXiv:1803.09655*, 2018.

[18] A. Antoniou, A. Storkey, and H. Edwards, "Data augmentation generative adversarial networks," *arXiv:1711.04340 [cs, stat]*, 2018-03-21.

[19] S. K. Lim, Y. Loo, N.-T. Tran, N.-M. Cheung, G. Roig, and Y. Elovici, "Doping: Generative data augmentation for unsupervised anomaly detection with gan," in *2018 IEEE International Conference on Data Mining (ICDM)*. IEEE, 2018, pp. 1122–1127.

[20] Y. Zhu, M. Aoun, M. Krijn, J. Vanschoren, and H. T. Campus, "Data Augmentation using Conditional Generative Adversarial Networks for Leaf Counting in Arabidopsis Plants." in *BMVC*, 2018, p. 324.

[21] X. Yi, E. Walia, and P. Babyn, "Generative adversarial network in medical imaging: A review," *Medical image analysis*, vol. 58, p. 101552, 2019.

[22] H.-C. Shin, N. A. Tenenholtz, J. K. Rogers, C. G. Schwarz, M. L. Senjem, J. L. Gunter, K. P. Andriole, and M. Michalski, "Medical image synthesis for data augmentation and anonymization using generative adversarial networks," in *International Workshop on Simulation and Synthesis in Medical Imaging*, ser. LNCS. Springer, 2018, pp. 1–11.

[23] F. Calimeri, A. Marzullo, C. Stamile, and G. Terracina, "Biomedical data augmentation using generative adversarial neural networks," in *International conference on artificial neural networks*. Springer, 2017, pp. 626–634.

[24] M. Frid-Adar, I. Diamant, E. Klang, M. Amitai, J. Goldberger, and H. Greenspan, "GAN-based synthetic medical image augmentation for increased CNN performance in liver lesion classification," *Neurocomputing*, vol. 321, pp. 321–331, 2018.

[25] V. Sandfort, K. Yan, P. J. Pickhardt, and R. M. Summers, "Data augmentation using generative adversarial networks (CycleGAN) to improve generalizability in CT segmentation tasks," *Scientific reports*, vol. 9, no. 1, p. 16884, 2019.

[26] A. Madani, M. Moradi, A. Karargyris, and T. Syeda-Mahmood, "Chest x-ray generation and data augmentation for cardiovascular abnormality classification," in *Medical Imaging 2018: Image Processing*, vol. 10574. International Society for Optics and Photonics, 2018, p. 105741M.

[27] H. Salehinejad, S. Valaee, T. Dowdell, E. Colak, and J. Barfett, "Generalization of deep neural networks for chest pathology classification in x-rays using generative adversarial networks," in *2018 IEEE International Conference on Acoustics, Speech and Signal Processing (ICASSP)*. IEEE, 2018, pp. 990–994.

[28] A. Waheed, M. Goyal, D. Gupta, A. Khanna, F. Al-Turjman, and P. R. Pinheiro, "Covidgan: data augmentation using auxiliary classifier gan for improved covid-19 detection," *Ieee Access*, vol. 8, pp. 91 916–91 923, 2020.

[29] L. Bi, J. Kim, A. Kumar, D. Feng, and M. Fulham, "Synthesis of Positron Emission Tomography (PET) Images via Multi-channel Generative Adversarial Networks (GANs)," in *Molecular Imaging, Reconstruction and Analysis of Moving Body Organs, and Stroke Imaging and Treatment*, ser. LNCS. Springer, 2017, pp. 43–51.

[30] Y. Liu, Y. Zhou, X. Liu, F. Dong, C. Wang, and Z. Wang, "Wasserstein gan-based small-sample augmentation for new-generation artificial intelligence: a case study of cancer-staging data in biology," *Engineering*, vol. 5, no. 1, pp. 156–163, 2019.

[31] C. Baur, S. Albarqouni, and N. Navab, "Generating highly realistic images of skin lesions with GANs," in *OR 2.0 Context-Aware Operating Theaters, Computer Assisted Robotic Endoscopy, Clinical Image-Based Procedures, and Skin Image Analysis*. Springer, 2018, pp. 260–267.

[32] D. Korkinof, T. Rijken, M. O'Neill, J. Yearsley, H. Harvey, and B. Glocker, "High-resolution mammogram synthesis using progressive generative adversarial networks," *arXiv preprint arXiv:1807.03401*, 2018.

[33] E. Wu, K. Wu, D. Cox, and W. Lotter, "Conditional infilling gans for data augmentation in mammogram classification," in *Image analysis for moving organ, breast, and thoracic images*. Springer, 2018, pp. 98–106.

[34] W.-N. Hsu, Y. Zhang, and J. Glass, "Unsupervised domain adaptation for robust speech recognition via variational autoencoder-based data augmentation," in *2017 IEEE Automatic Speech Recognition and Understanding Workshop (ASRU)*. IEEE, 2017, pp. 16–23.

[35] H. Nishizaki, "Data augmentation and feature extraction using variational autoencoder for acoustic modeling," in *2017 Asia-Pacific Signal and Information Processing Association Annual Summit and Conference (APSIPA ASC)*. IEEE, 2017, pp. 1222–1227.

[36] Z. Wu, S. Wang, Y. Qian, and K. Yu, "Data augmentation using variational autoencoder for embedding based speaker verification," in *Interspeech 2019*. ISCA, 2019, pp. 1163–1167.

[37] P. Zhuang, A. G. Schwing, and O. Koyejo, "Fmri data augmentation via synthesis," in *2019 IEEE 16th International Symposium on Biomedical Imaging (ISBI 2019)*. IEEE, 2019, pp. 1783–1787.

[38] X. Liu, Y. Zou, L. Kong, Z. Diao, J. Yan, J. Wang, S. Li, P. Jia, and J. You, "Data augmentation via latent space interpolation for image classification," in *2018 24th International Conference on Pattern Recognition (ICPR)*. IEEE, 2018, pp. 728–733.

[39] N. Painchaud, Y. Skandarani, T. Judge, O. Bernard, A. Lalande, and P.-M. Jodoin, "Cardiac mri segmentation with strong anatomical guarantees," in *International Conference on Medical Image Computing and Computer-Assisted Intervention*. Springer, 2019, pp. 632–640.

[40] R. Selvan, E. B. Dam, N. S. Detlefsen, S. Rischel, K. Sheng, M. Nielsen, and A. Pai, "Lung segmentation from chest x-rays using variational data imputation," *arXiv:2005.10052 [cs, eess, stat]*, 2020.

[41] A. Myronenko, "3d mri brain tumor segmentation using autoencoder regularization," in *International MICCAI Brainlesion Workshop*. Springer, 2018, pp. 311–320.

[42] M. I. Jordan, Z. Ghahramani, T. S. Jaakkola, and L. K. Saul, "An introduction to variational methods for graphical models," *Machine Learning*, vol. 37, no. 2, pp. 183–233, 1999.

[43] Y. Burda, R. Grosse, and R. Salakhutdinov, "Importance weighted autoencoders," *arXiv:1509.00519 [cs, stat]*, 2016-11-07.

[44] A. A. Alemi, I. Fischer, J. V. Dillon, and K. Murphy, "Deep variational information bottleneck," *arXiv preprint arXiv:1612.00410*, 2016.

[45] I. Higgins, L. Matthey, A. Pal, C. Burgess, X. Glorot, M. Botvinick, S. Mohamed, and A. Lerchner, "beta-VAE: Learning basic visual concepts with a constrained variational framework." *ICLR*, vol. 2, no. 5, p. 6, 2017.

[46] C. Cremer, X. Li, and D. Duvenaud, "Inference suboptimality in

variational autoencoders," in *International Conference on Machine Learning*. PMLR, 2018, pp. 1078–1086.

[47] C. Zhang, J. Bütepage, H. Kjellström, and S. Mandt, "Advances in variational inference," *IEEE Transactions on Pattern Analysis and Machine Intelligence*, vol. 41, no. 8, pp. 2008–2026, 2018.

[48] F. Ruiz and M. Titsias, "A contrastive divergence for combining variational inference and mcmc," in *International Conference on Machine Learning*. PMLR, 2019, pp. 5537–5545.

[49] T. Salimans, D. Kingma, and M. Welling, "Markov chain monte carlo and variational inference: Bridging the gap," in *International Conference on Machine Learning*, 2015, pp. 1218–1226.

[50] D. Rezende and S. Mohamed, "Variational inference with normalizing flows," in *International Conference on Machine Learning*. PMLR, 2015, pp. 1530–1538.

[51] R. M. Neal and others, "MCMC using hamiltonian dynamics," *Handbook of Markov Chain Monte Carlo*, vol. 2, no. 11, p. 2, 2011.

[52] A. L. Caterini, A. Doucet, and D. Sejdinovic, "Hamiltonian variational auto-encoder," in *Advances in Neural Information Processing Systems*, 2018, pp. 8167–8177.

[53] M. D. Hoffman and M. J. Johnson, "Elbo surgery: yet another way to carve up the variational evidence lower bound," in *Workshop in Advances in Approximate Bayesian Inference, NIPS*, vol. 1, 2016, p. 2.

[54] E. Nalisnick, L. Hertel, and P. Smyth, "Approximate inference for deep latent gaussian mixtures," in *NIPS Workshop on Bayesian Deep Learning*, vol. 2, 2016, p. 131.

[55] N. Dilokthanakul, P. A. M. Mediano, M. Garnelo, M. C. H. Lee, H. Salimbeni, K. Arulkumaran, and M. Shanahan, "Deep unsupervised clustering with gaussian mixture variational autoencoders," *arXiv:1611.02648 [cs, stat]*, 2017.

[56] J. Tomczak and M. Welling, "Vae with a vampprior," in *International Conference on Artificial Intelligence and Statistics*. PMLR, 2018, pp. 1214–1223.

[57] C. K. Sønderby, T. Raiko, L. Maaløe, S. K. Sønderby, and O. Winther, "Ladder variational autoencoder," in *29th Annual Conference on Neural Information Processing Systems (NIPS 2016)*, 2016.

[58] A. Klushyn, N. Chen, R. Kurle, and B. Cseke, "Learning Hierarchical Priors in VAEs," *Advances in neural information processing systems*, p. 10, 2019.

[59] X. Chen, D. P. Kingma, T. Salimans, Y. Duan, P. Dhariwal, J. Schulman, I. Sutskever, and P. Abbeel, "Variational lossy autoencoder," *arXiv preprint arXiv:1611.02731*, 2016.

[60] A. Razavi, A. v. d. Oord, and O. Vinyals, "Generating diverse high-fidelity images with vq-vae-2," *Advances in Neural Information Processing Systems*, 2020.

[61] B. Pang, T. Han, E. Nijkamp, S.-C. Zhu, and Y. N. Wu, "Learning latent space energy-based prior model," *Advances in Neural Information Processing Systems*, vol. 33, 2020.

[62] J. Aneja, A. Schwing, J. Kautz, and A. Vahdat, "NCP-VAE: Variational autoencoders with noise contrastive priors," *arXiv:2010.02917 [cs, stat]*, 2020.

[63] M. Bauer and A. Mnih, "Resampled priors for variational autoencoders," in *The 22nd International Conference on Artificial Intelligence and Statistics*. PMLR, 2019, pp. 66–75.

[64] T. R. Davidson, L. Falorsi, N. De Cao, T. Kipf, and J. M. Tomczak, "Hyperspherical variational auto-encoders," in *34th Conference on Uncertainty in Artificial Intelligence 2018, UAI 2018*. Association For Uncertainty in Artificial Intelligence (AUAI), 2018, pp. 856–865.

[65] E. Mathieu, C. Le Lan, C. J. Maddison, R. Tomioka, and Y. W. Teh, "Continuous hierarchical representations with poincaré variational auto-encoders," in *Advances in neural information processing systems*, 2019, pp. 12 565–12 576.

[66] I. Ovinnikov, "Poincaré wasserstein autoencoder," *arXiv:1901.01427 [cs, stat]*, 2020-03-16.

[67] L. Falorsi, P. de Haan, T. R. Davidson, N. De Cao, M. Weiler, P. Forré, and T. S. Cohen, "Explorations in homeomorphic variational auto-encoding," *arXiv:1807.04689 [cs, stat]*, 2018.

[68] N. Miolane and S. Holmes, "Learning weighted submanifolds with variational autoencoders and riemannian variational autoencoders," in *Proceedings of the IEEE/CVF Conference on Computer Vision and Pattern Recognition*, 2020, pp. 14 503–14 511.

[69] G. Arvanitidis, L. K. Hansen, and S. Hauberg, "A locally adaptive normal distribution," *Advances in Neural Information Processing Systems*, pp. 4258–4266, 2016.

[70] N. Chen, A. Klushyn, R. Kurle, X. Jiang, J. Bayer, and P. Smagt, "Metrics for deep generative models," in *International Conference on Artificial Intelligence and Statistics*. PMLR, 2018, pp. 1540–1550.

[71] H. Shao, A. Kumar, and P. T. Fletcher, "The riemannian geometry of deep generative models," in *2018 IEEE/CVF Conference on Computer Vision and Pattern Recognition Workshops (CVPRW)*. IEEE, 2018, pp. 428–4288.

[72] D. Kalatzis, D. Eklund, G. Arvanitidis, and S. Hauberg, "Variational autoencoders with riemannian brownian motion priors," in *International Conference on Machine Learning*. PMLR, 2020, pp. 5053–5066.

[73] C. Chadebec, C. Mantoux, and S. Allassonnière, "Geometry-aware hamiltonian variational auto-encoder," *arXiv:2010.11518 [cs, math, stat]*, 2020.

[74] G. Arvanitidis, B. Georgiev, and B. Schölkopf, "A prior-based approximate latent riemannian metric," *arXiv:2103.05290 [cs, stat]*, 2021.

[75] G. Arvanitidis, L. K. Hansen, and S. Hauberg, "Latent space oddity: On the curvature of deep generative models," in *6th International Conference on Learning Representations, ICLR 2018*, 2018.

[76] M. F. Frenzel, B. Teleaga, and A. Ushio, "Latent space cartography: Generalised metric-inspired measures and measure-based transformations for generative models," *arXiv preprint arXiv:1902.02113*, 2019.

[77] G. Arvanitidis, S. Hauberg, and B. Schölkopf, "Geometrically enriched latent spaces," *arXiv:2008.00565 [cs, stat]*, 2020-08-02.

[78] G. Lebanon, "Metric learning for text documents," *IEEE Transactions on Pattern Analysis and Machine Intelligence*, vol. 28, no. 4, pp. 497–508, 2006.

[79] M. Louis, "Computational and statistical methods for trajectory analysis in a Riemannian geometry setting," PhD Thesis, Sorbonnes universités, 2019.

[80] M. Girolami, B. Calderhead, and S. A. Chin, "Riemannian manifold hamiltonian monte carlo," *arXiv preprint arXiv:0907.1100*, 2009.

[81] M. Girolami and B. Calderhead, "Riemann manifold langevin and hamiltonian monte carlo methods," *Journal of the Royal Statistical Society: Series B (Statistical Methodology)*, vol. 73, no. 2, pp. 123–214, 2011.

[82] A. Paszke, S. Gross, S. Chintala, G. Chanan, E. Yang, Z. DeVito, Z. Lin, A. Desmaison, L. Antiga, and A. Lerer, "Automatic differentiation in pytorch," 2017.

[83] R. M. Neal, "Hamiltonian importance sampling," in *talk presented at the Banff International Research Station (BIRS) workshop on Mathematical Issues in Molecular Dynamics*, 2005.

[84] S. Duane, A. D. Kennedy, B. J. Pendleton, and D. Roweth, "Hybrid monte carlo," *Physics Letters B*, vol. 195, no. 2, pp. 216–222, 1987.

[85] B. Leimkuhler and S. Reich, *Simulating hamiltonian dynamics*. Cambridge university press, 2004, vol. 14.

[86] J. S. Liu, *Monte Carlo strategies in scientific computing*. Springer Science & Business Media, 2008.

[87] M. Arjovsky, S. Chintala, and L. Bottou, "Wasserstein GAN," *arXiv:1701.07875 [cs, stat]*, 2017-12-06.

[88] H. Xiao, K. Rasul, and R. Vollgraf, "Fashion-mnist: a novel image dataset for benchmarking machine learning algorithms," *arXiv preprint arXiv:1708.07747*, 2017.

[89] G. Cohen, S. Afshar, J. Tapson, and A. Van Schaik, "Emnist: Extending mnist to handwritten letters," in *2017 International Joint Conference on Neural Networks (IJCNN)*. IEEE, 2017, pp. 2921–2926.

[90] Y. LeCun, "The MNIST database of handwritten digits," 1998.

[91] T. Salimans, I. Goodfellow, W. Zaremba, V. Cheung, A. Radford, and X. Chen, "Improved techniques for training gans," in *Advances in Neural Information Processing Systems*, 2016.

[92] M. Heusel, H. Ramsauer, T. Unterthiner, B. Nessler, and S. Hochreiter, "Gans trained by a two time-scale update rule converge to a local nash equilibrium," in *Advances in Neural Information Processing Systems*, 2017.

[93] T. Karras, T. Aila, S. Laine, and J. Lehtinen, "Progressive growing of gans for improved quality, stability, and variation," in *International Conference on Learning Representations (ICLR)*, 2017.

[94] M. Lucic, K. Kurach, M. Michalski, S. Gelly, and O. Bousquet, "Are GANs created equal? a large-scale study," in *Advances in Neural Information Processing Systems*, 2018, p. 10.

[95] K. Shmelkov, C. Schmid, and K. Alahari, "How good is my gan?" in *Proceedings of the European Conference on Computer Vision (ECCV)*, 2018, pp. 213–229.

[96] A. Borji, "Pros and cons of GAN evaluation measures," *Computer Vision and Image Understanding*, vol. 179, pp. 41–65, 2019.

[97] G. Huang, Z. Liu, L. Van Der Maaten, and K. Q. Weinberger, "Densely connected convolutional networks," in *2017 IEEE Conference on Computer Vision and Pattern Recognition (CVPR)*. IEEE, 2017, pp. 2261–2269.

[98] B. Amos, "bamos/densenet.pytorch," 2020, original-date: 2017-02-09T15:33:23Z. [Online]. Available: https://github.com/bamos/densenet.pytorch

[99] L. Breiman, "Random forests," *Machine Learning*, vol. 45, no. 1, pp. 5–32, 2001.

[100] S. B. Kotsiantis, I. Zaharakis, and P. Pintelas, "Supervised machine learning: A review of classification techniques," *Emerging artificial intelligence applications in computer engineering*, vol. 160, no. 1, pp. 3–24, 2007.

[101] J. Wen, E. Thibeau-Sutre, M. Diaz-Melo, J. Samper-González, A. Routier, S. Bottani, D. Dormont, S. Durrleman, N. Burgos, and O. Colliot, "Convolutional neural networks for classification of Alzheimer's disease: Overview and reproducible evaluation," *Medical Image Analysis*, vol. 63, p. 101694, 2020.

[102] K. Aderghal, M. Boissenin, J. Benois-Pineau, G. Catheline, and K. Afdel, "Classification of sMRI for AD diagnosis with convolutional neuronal networks: A pilot 2-D+ϵ study on ADNI," in *Lecture Notes in Computer Science (including subseries Lecture Notes in Artificial Intelligence and Lecture Notes in Bioinformatics)*, vol. 10132 LNCS, 2017, pp. 690–701.

[103] K. Aderghal, A. Khvostikov, A. Krylov, J. Benois-Pineau, K. Afdel, and G. Catheline, "Classification of Alzheimer Disease on Imaging Modalities with Deep CNNs Using Cross-Modal Transfer Learning," in *2018 IEEE 31st International Symposium on Computer-Based Medical Systems (CBMS)*, 2018, pp. 345–350, iSSN: 2372-9198.

[104] J. Islam and Y. Zhang, "GAN-based synthetic brain PET image generation," *Brain Informatics*, vol. 7, no. 1, 2020.

[105] K. Oh, Y.-C. Chung, K. W. Kim, W.-S. Kim, and I.-S. Oh, "Classification and Visualization of Alzheimer's Disease using Volumetric Convolutional Neural Network and Transfer Learning," *Scientific Reports*, vol. 9, no. 1, p. 18150, 2019.

[106] M. Liu, J. Zhang, C. Lian, and D. Shen, "Weakly Supervised Deep Learning for Brain Disease Prognosis Using MRI and Incomplete Clinical Scores," *IEEE Transactions on Cybernetics*, vol. 50, no. 7, pp. 3381–3392, 2020.

[107] A. Valliani and A. Soni, "Deep Residual Nets for Improved Alzheimer's Diagnosis," in *8th ACM International Conference on Bioinformatics, Computational Biology,and Health Informatics - ACM-BCB '17*. Boston, Massachusetts, USA: ACM Press, 2017, pp. 615–615.

[108] K. Backstrom, M. Nazari, I.-H. Gu, and A. Jakola, "An efficient 3D deep convolutional network for Alzheimer's disease diagnosis using MR images," in *2018 IEEE 15th International Symposium on Biomedical Imaging (ISBI 2018)*, vol. 2018-April, 2018, pp. 149–153.

[109] D. Cheng and M. Liu, "CNNs based multi-modality classification for AD diagnosis," in *2017 10th International Congress on Image and Signal Processing, BioMedical Engineering and Informatics (CISP-BMEI)*, 2017, pp. 1–5.

[110] K. A. Ellis, A. I. Bush, D. Darby, D. De Fazio, J. Foster, P. Hudson, N. T. Lautenschlager, N. Lenzo, R. N. Martins, P. Maruff, C. Masters, A. Milner, K. Pike, C. Rowe, G. Savage, C. Szoeke, K. Taddei, V. Villemagne, M. Woodward, D. Ames, and AIBL Research Group, "The Australian Imaging, Biomarkers and Lifestyle (AIBL) study of aging: methodology and baseline characteristics of 1112 individuals recruited for a longitudinal study of Alzheimer's disease," *International Psychogeriatrics*, vol. 21, no. 4, pp. 672–687, 2009.

[111] K. J. Gorgolewski, T. Auer, V. D. Calhoun, R. C. Craddock, S. Das, E. P. Duff, G. Flandin, S. S. Ghosh, T. Glatard, Y. O. Halchenko, D. A. Handwerker, M. Hanke, D. Keator, X. Li, Z. Michael, C. Maumet, B. N. Nichols, T. E. Nichols, J. Pellman, J.-B. Poline, A. Rokem, G. Schaefer, V. Sochat, W. Triplett, J. A. Turner, G. Varoquaux, and R. A. Poldrack, "The brain imaging data structure, a format for organizing and describing outputs of neuroimaging experiments," *Scientific Data*, vol. 3, no. 1, p. 160044, 2016.

[112] N. J. Tustison, B. B. Avants, P. A. Cook, Yuanjie Zheng, A. Egan, P. A. Yushkevich, and J. C. Gee, "N4ITK: Improved N3 Bias Correction," *IEEE Transactions on Medical Imaging*, vol. 29, no. 6, pp. 1310–1320, 2010.

[113] V. Fonov, A. Evans, R. McKinstry, C. Almli, and D. Collins, "Unbiased nonlinear average age-appropriate brain templates from birth to adulthood," *NeuroImage*, vol. 47, p. S102, 2009.

[114] V. Fonov, A. C. Evans, K. Botteron, C. R. Almli, R. C. McKinstry, and D. L. Collins, "Unbiased average age-appropriate atlases for pediatric studies," *NeuroImage*, vol. 54, no. 1, pp. 313–327, 2011.

[115] B. B. Avants, N. J. Tustison, M. Stauffer, G. Song, B. Wu, and J. C. Gee, "The Insight ToolKit image registration framework," *Frontiers in Neuroinformatics*, vol. 8, 2014.

[116] V. S. Fonov, M. Dadar, T. P.-A. R. Group, and D. L. Collins, "Deep learning of quality control for stereotaxic registration of human brain MRI," *bioRxiv*, p. 303487, 2018.

[117] J. Bergstra and Y. Bengio, "Random Search for Hyper-Parameter Optimization," *Journal of Machine Learning Research*, vol. 13, no. Feb, pp. 281–305, 2012.

[118] K. He, X. Zhang, S. Ren, and J. Sun, "Delving Deep into Rectifiers: Surpassing Human-Level Performance on ImageNet Classification," in *2015 IEEE International Conference on Computer Vision (ICCV)*. Santiago, Chile: IEEE, 2015, pp. 1026–1034.

[119] D. P. Kingma and J. Ba, "Adam: A method for stochastic optimization," *arXiv preprint arXiv:1412.6980*, 2014.

Clément Chadebec is a PhD student funded by $PR[AI]RIE$ at Université de Paris and Inria. His research interests include machine learning, Riemannian geometry and computational statistics for medicine. He received master degrees from Ecole Nationale des Mines de Paris and Ecole Normale Supérieure Paris-Saclay.

Elina Thibeau-Sutre is a PhD student at Sorbonne Université and Inria. Her research interest include deep learning application to neuroimaging data, its interpretability and reproducibility. She received master degrees from Ecole Nationale des Mines de Paris and Ecole supérieure de physique et de chimie industrielles (Paris, France).

Ninon Burgos CNRS researcher in the ARAMIS Lab, a joint laboratory between Sorbonne Université, CNRS, Inserm and Inria within the Paris Brain Institute, France. She completed her PhD at University College London, UK, in 2016. Her research focuses on the development of computational imaging tools to improve the understanding and diagnosis of dementia.

Stéphanie Allassonnière Pr. of Applied Mathematics in Université de Paris, $PR[AI]RIE$ fellow and deputy directeor. She received her PhD degree in Applied Mathematics (2007), studies one year as postdoctoral fellow in the CIS, JHU, Baltimore. She then joined the Applied Mathematics department of Ecole Polytechnique in 2008 as assistant professor and moved to Paris Descartes school of medicine in 2016 as Professor. Her researches focus on statistical analysis of medical databases in order to: understanding the common features of populations, designing classification, early prediction and decision support systems.

APPENDIX A
PROOF OF PROP. 1

Proposition 2. The Riemannian manifold $(\mathbb{R}^d, g)$ is *geodesic ally complete*.

We will show that given the manifold $\mathcal{M} = \mathbb{R}^d$ endowed with the Riemannian metric g whose local representation is given by:

$$\mathbf{G}^{-1}(z) = \sum_{i=1}^{N} L_{\psi_i} L_{\psi_i}^\top \exp\Big(-\frac{\|z-c_i\|_2^2}{T^2}\Big) + \lambda I_d \qquad (7)$$

or Eq. (4) in the paper, any geodesic curve $\gamma :]a,b[\to \mathcal{M}$ is actually extensible to $\mathbb{R}$ that is the Riemannian manifold $(\mathbb{R}^d, g)$ is *geodesically complete*. The proof we derive is inspired from the one proposed in [79].

Proof: Let us suppose that there exists a geodesic curve γ such that it cannot be extended to $\mathbb{R}$. Therefore, there exist $a, b \in \mathbb{R}$ such that $I =]a,b[$ is the domain of definition of $\gamma : I \to \mathcal{M}$. We show that such an assumption leads to an absurdity.

First, since L_{ψ_i} are defined as lower triangular matrices with positive diagonal coefficients we have that $L_{\psi_i} L_{\psi_i}^\top$ is a symmetric positive-definite matrix (by Cholesky decomposition). Therefore, $x^\top L_{\psi_i} L_{\psi_i}^\top x > 0,\ \forall\, x \in \mathbf{R}^d - \{0\}$.

Then, let $t \in]a,b[$, we recall that

$$\|\dot\gamma(t)\|^2_{\gamma(t)} = \langle \dot\gamma(t) | \dot\gamma(t) \rangle_{\gamma(t)} = \dot\gamma(t)^\top \mathbf{G}(\gamma(t)) \dot\gamma(t)\,.$$

Hence, let $t_0 \in]a,b[$. For any $t \in]a,b[$,

$$\begin{aligned}\|\dot\gamma(t)\|_2^2 &\le \|\dot\gamma(t)\|_2^2 + \\ &\frac{1}{\lambda}\sum_{i=1}^{N} \dot\gamma(t)^\top L_{\psi_i} L_{\psi_i}^\top \dot\gamma(t) \exp\left(-\frac{\|\gamma(t)-c_i\|_2^2}{T^2}\right) \\ &\le \frac{1}{\lambda}\cdot \|\dot\gamma(t)\|^2_{\gamma(t)} = \frac{1}{\lambda}\cdot \|\dot\gamma(t_0)\|^2_{\gamma(t_0)}\,,\end{aligned}$$

where the last equality comes for the constant speed of geodesic curves. Therefore

$$\|\gamma(t) - \gamma(t_0)\|_2 \le \frac{\|\dot\gamma(t_0)\|_{\gamma(t_0)}}{\sqrt{\lambda}} \cdot |t - t_0|\,.$$

This shows that for any $t \in]a,b[$ the geodesic curve γ remains within a compact set and so γ is bounded on I. Now consider the sequence $t_n \xrightarrow[n\to\infty]{} b$. As geodesic curves have constant speed, $I = \{(t_n, \dot\gamma(t_n))\}_{n\in\mathbb{N}}$ is a compact set. Moreover, by application of Cauchy-Lipschitz theorem, one can find $\varepsilon > 0$ such that for any $n \in \mathbb{N}$, γ can be defined on $]t_n - \varepsilon, t_n + \varepsilon[$. Since t_n can be as close to b as desired, there exists $N \in \mathbb{N}$ such that $\forall n \ge N$ we have $t_n \ge b - \frac{\varepsilon}{2}$. This means that the domain of definition of the curve γ can be extended to $]a, b + \frac{\varepsilon}{2}[$ which concludes the proof. □

APPENDIX B
DETAILED EXPERIMENTAL SETTING

B.1 Parameters of Sec. 3.3. Generation Comparison

For this experiment, we consider a vanilla VAE, a VAE with VAMP prior and a *geometry-aware* VAE. For a fair comparison, each model is trained with the same neural network architecture for the encoder and decoder along with the same latent space dimension. The main parameters for the *geometry-aware* VAE are presented in Table. 8. We refer the reader to [73] for a more precise description of each of these parameters and their impact on the model. For the VAMP prior the number of pseudo-inputs is set to 10 and we use the implementation provided by the authors. Each model is trained until the ELBO does not improve for 20 epochs with an Adam optimizer [119] and a learning rate of 10^{-3}. Since the data sets sizes are small the training is performed in a single batch.

TABLE 7
Neural Net Architectures. The same architectures are used for the vanilla VAE, VAMP - VAE and *geometry-aware* VAEs.

μ_ϕ Σ_ϕ	(D, 400, relu)	(400, d, linear) (400, d, linear)
π_θ	(d, 400, relu)	(400, D, sigmoid)
$L_\psi^{\text{diag.}}$ $L_\psi^{\text{low.}}$	(D, 400, relu)	(400, d, linear) (400, $\frac{d(d-1)}{2}$, linear)

D: Input space dimension
d: Latent space dimension

TABLE 8
Geometry-aware VAE parameters.

Data sets	Parameters					
	d^*	n_{lf}	ε_{lf}	T	λ	$\sqrt{\beta_0}$
Synthetic shapes	2	3	10^{-2}	0.8	10^{-3}	0.3
reduced MNIST (bal.)	2	3	10^{-2}	0.8	10^{-3}	0.3
reduced MNIST (unbal.)	2	3	10^{-2}	0.8	10^{-3}	0.3
reduced EMNIST	2	3	10^{-2}	0.8	10^{-3}	0.3

* Latent space dimension (same for VAE and VAMP-VAE)

B.2 Parameters of Sec. 4. Data Augmentation

For this experiment, the same parameters and neural networks architectures as presented in the former section are used except for *reduced* Fashion where the dimension of the latent space is set to 5. As to training parameters for the VAEs, for each model we use an Adam optimizer with a learning rate set to 10^{-3}. Since the data sets sizes are small the training is performed in a single batch. As to the DenseNet [97] used as benchmark for data augmentation, the implementation we use is the one in [98] with a *growth rate* equals to 10, *depth* of 20 and 0.5 *reduction* and is trained with a learning rate of 10^{-3}, weight decay of 10^{-4} and a batch size of 200. The classifier is trained until the loss does not improve on the validation set for 50 epochs and tested on the original test sets (*e.g.* ≈ 1000 samples for MNIST). For Sec. 4.2.3., the MLP has 400 hidden units with relu activation function. It is trained with Adam optimizer and a learning rate of 10^{-3}. Training is stopped if the loss does not improve on the validation set for 20 epochs

B.3 Parameters of Sec. 5 Validation on Medical Imaging

To generate new data on the ADNI database we amend the neural network architectures and use the one described in Table. 9. The parameters used in the *geometry-aware* VAE are provided in Table. 10. An Adam optimizer with a learning rate of 10^{-5} and batch size of 25 are used. The VAE model is trained until the ELBO does not improve for 50 epochs. Generating 50 ADNI images takes approx. 30 s.[5] with the proposed method on Intel Core i7 CPU (6x1.1GHz) and 16 GB RAM.

TABLE 9
Neural Net Architecture

μ_ϕ	(D, h1, rel)	(h1, h2, relu)	(h2, h3, relu)	(h3, d, lin)
Σ_ϕ		(h1, h2, relu)	(h2, h3, relu)	(h3, d, lin)
π_θ	(d, h3, relu)	(h3, h2, relu)	(h2, h1, relu)	(h1, D, sig)
$L_\psi^{\text{diag.}}$	(D, h3, relu)	(h3, d, lin)	-	-
$L_\psi^{\text{low.}}$		(h3, $\frac{d(d-1)}{2}$, lin)	-	-
D	h1	h2	h3	d
777504	500	500	400	10

TABLE 10
Geometry-aware parameters settings for ADNI database

Data set	Parameters					
	d	n_{lf}	ε_{lf}	T	λ	$\sqrt{\beta_0}$
ADNI	10	3	10^{-3}	1.5	10^{-2}	0.3

APPENDIX C
A FEW MORE SAMPLING COMPARISONS (SEC. 3.3)

In addition to the comparison performed in Sec. 3.3.1, we also compare qualitatively a Vanilla VAE, a VAE with VAMP prior and a *geometry-aware* VAE on 4 reduced data sets and in higher dimensional latent spaces of dimension 10. The first one is created with 180 binary rings and circles with different diameters and thicknesses ensuring balanced classes. The second one is composed of 120 samples of EMNIST (letter *M*) and referred to as *reduced* EMNIST. Another one is created with 120 samples from the classes *1*, *2* and *3* of MNIST database ensuring balanced classes and is called *reduced* MNIST. The last one, *reduced* Fashion, is again composed of 120 samples from 3 classes (*shoes*, *trouser* and *bag*) from FashionMNIST and ensuring balanced classes. The models have the same architectures as described in Table. 7 and are trained with the parameters stated in Table. 11. 10 pseudo-inputs are again used to train the VAE with VAMP prior. Each model is trained until the ELBO does not improve for 20 epochs with Adam optimizer, a learning rate of 10^{-3} and in a single batch. In Fig. 10 are presented from top to bottom: 1) an extract of the training samples for each data set; 2) samples obtained with a vanilla VAE with a Gaussian prior; 2) data generated from a VAE with VAMP prior; 3) samples created by a *geometry-aware* VAE and using the prior or 4) samples from our method. As discussed in the paper, the proposed method is again able to visually outperform peers since for all data sets it is able to create sharper and more meaningful samples even if the number of training samples is quite small.

5. Depends on the length of the MCMC chain and HMC hyper-parameter, l. We used 300 steps with $l = 15$.

TABLE 11
Geometry-aware VAE parameters.

Data sets	Parameters					
	d^*	n_{lf}	ε_{lf}	T	λ	$\sqrt{\beta_0}$
Synthetic shapes	10	3	10^{-2}	1.5	10^{-3}	0.3
reduced MNIST	10	3	10^{-2}	1.5	10^{-3}	0.3
reduced EMNIST	10	3	10^{-2}	1.5	10^{-3}	0.3
reduced Fashion	10	3	10^{-2}	1.5	10^{-3}	0.3

* Latent space dimension (same for VAE and VAMP-VAE)

APPENDIX D
ADDITIONAL RESULTS (SEC.4.2.3)

Further to the experiments presented in Sec. 4.2.3, we also provide the results of the 4 classifiers on *reduced* EMNIST and *reduced* Fashion in Fig. 9. Again, for most classifiers the proposed method either equals or greatly outperform the *baseline*.

APPENDIX E
A FEW MORE SAMPLE GENERATION ON ADNI

In this section, we first provide several slices of a 3D image generated by our model. The model is trained on the class AD of *train-50* (*i.e.* on 50 MRI of patient having been diagnosed with Alzheimer disease). The generated image is presented in Fig. 11. We also present in Fig. 12, 4 generated patients for a model trained on *train-50*. The two left images show *cognitively normal* generated patients while the rightmost images represent AD generated patients.

APPENDIX F
THE INTRUDERS: ANSWERS TO FIG. 7

In Fig. 7 of the paper, the synthetic samples are the leftmost and rightmost images while the *real* patients are in the middle. The model is trained on the class AD of *train-full* *i.e.* 210 images.

APPENDIX G
COMPLEMENTARY RESULTS ON MEDICAL IMAGES

Results on synthetic data only for the classification task on MRIs are added in tables 12 to 15. As observed on the *toy* examples, the proposed model is again able to produce meaningful synthetic samples since each CNN outperforms greatly the *baseline* (*i.e.* the real training data) either on *train-50* or *train-full*. The fact that classification performances on AIBL (which is never used for training) are better for a classifier trained on synthetic data than on the *baseline* shows again that the generative model does not overfit the training data (coming from ADNI) but rather produces samples that are also relevant for another database.

TABLE 12
Mean test performance of the 20 runs trained on *train-50* with the baseline hyperparameters

		ADNI			AIBL		
image type	synthetic images	sensitivity	specificity	balanced accuracy	sensitivity	specificity	balanced accuracy
real	-	70.3 ± 12.2	62.4 ± 11.5	66.3 ± 2.4	60.7 ± 13.7	73.8 ± 7.2	67.2 ± 4.1
real (high-resolution)	-	78.5 ± 9.4	57.4 ± 8.8	67.9 ± 2.3	57.2 ± 11.2	75.8 ± 7.0	66.5 ± 3.0
synthetic	500	72.4 ± 6.4	65.6 ± 8.1	69.0 ± 1.9	56.6 ± 9.9	80.0 ± 5.3	68.3 ± 3.0
synthetic	1000	75.0 ± 6.2	65.6 ± 7.4	70.3 ± 2.0	62.7 ± 9.7	78.8 ± 5.3	70.8 ± 3.5
synthetic	2000	71.4 ± 6.6	70.4 ± 6.6	70.9 ± 3.0	62.1 ± 8.8	80.5 ± 4.7	71.3 ± 3.6
synthetic	3000	70.6 ± 5.2	$\mathbf{73.8 \pm 4.2}$	72.2 ± 1.4	65.7 ± 6.9	80.5 ± 4.6	73.1 ± 1.8
synthetic	5000	$\mathbf{78.1 \pm 6.1}$	69.0 ± 6.9	73.5 ± 2.0	$\mathbf{74.5 \pm 7.8}$	77.3 ± 5.4	$\mathbf{76.5 \pm 2.9}$
synthetic	10000	75.2 ± 6.8	73.4 ± 4.8	$\mathbf{74.3 \pm 1.9}$	73.6 ± 10.8	$\mathbf{79.4 \pm 6.0}$	75.9 ± 2.5
synthetic + real	500	71.9 ± 5.3	67.0 ± 4.5	69.4 ± 1.6	55.9 ± 6.8	81.1 ± 3.1	68.5 ± 2.5
synthetic + real	1000	69.8 ± 6.6	71.2 ± 3.7	70.5 ± 2.1	59.1 ± 9.0	82.1 ± 3.7	70.6 ± 3.1
synthetic + real	2000	72.2 ± 4.4	70.3 ± 4.3	71.2 ± 1.6	66.6 ± 7.1	79.0 ± 4.1	72.8 ± 2.2
synthetic + real	3000	71.8 ± 4.9	73.4 ± 5.5	72.6 ± 1.6	66.1 ± 9.3	81.1 ± 5.0	73.6 ± 3.0
synthetic + real	5000	$\mathbf{74.7 \pm 5.3}$	$\mathbf{73.5 \pm 4.8}$	$\mathbf{74.1 \pm 2.2}$	$\mathbf{71.7 \pm 10.0}$	80.5 ± 4.4	$\mathbf{76.1 \pm 3.6}$
synthetic + real	10000	74.7 ± 7.0	73.4 ± 6.1	74.0 ± 2.7	69.1 ± 9.9	$\mathbf{80.7 \pm 5.1}$	74.9 ± 3.2

TABLE 13
Mean test performance of the 20 runs trained on *train-full* with the baseline hyperparameters

		ADNI			AIBL		
image type	synthetic images	sensitivity	specificity	balanced accuracy	sensitivity	specificity	balanced accuracy
real	-	79.1 ± 6.2	76.3 ± 4.2	77.7 ± 2.5	70.6 ± 6.7	86.3 ± 3.6	78.4 ± 2.4
real (high-resolution)	-	84.5 ± 3.8	76.7 ± 4.0	80.6 ± 1.1	71.6 ± 6.4	89.2 ± 2.7	80.4 ± 2.6
synthetic	500	81.6 ± 6.8	79.5 ± 5.8	80.5 ± 2.4	74.7 ± 9.3	87.3 ± 4.8	81.0 ± 3.2
synthetic	1000	82.9 ± 4.5	82.0 ± 5.8	82.4 ± 1.9	77.2 ± 7.4	88.8 ± 5.2	83.0 ± 2.0
synthetic	2000	81.9 ± 4.5	87.7 ± 3.4	84.8 ± 2.0	74.7 ± 6.3	92.1 ± 1.9	83.4 ± 2.7
synthetic	3000	$\mathbf{84.9 \pm 3.5}$	87.4 ± 3.5	86.1 ± 1.5	77.4 ± 5.8	90.9 ± 3.0	84.2 ± 1.8
synthetic	5000	84.0 ± 3.5	88.4 ± 3.3	86.2 ± 1.7	76.8 ± 4.2	$\mathbf{92.2 \pm 1.8}$	$\mathbf{84.5 \pm 1.8}$
synthetic	10000	84.2 ± 5.4	$\mathbf{88.6 \pm 3.9}$	$\mathbf{86.4 \pm 1.8}$	$\mathbf{77.5 \pm 7.4}$	91.0 ± 3.2	84.2 ± 2.4
synthetic + real	500	82.5 ± 3.4	81.9 ± 5.4	82.2 ± 2.4	76.0 ± 6.3	89.7 ± 3.3	82.9 ± 2.5
synthetic + real	1000	84.6 ± 4.4	84.3 ± 5.1	84.4 ± 1.8	77.0 ± 7.0	90.4 ± 3.4	83.7 ± 2.3
synthetic + real	2000	$\mathbf{85.4 \pm 4.0}$	86.4 ± 5.9	85.9 ± 1.6	77.2 ± 6.9	90.4 ± 3.8	83.8 ± 2.2
synthetic + real	3000	84.7 ± 3.6	86.8 ± 4.5	85.8 ± 1.7	77.2 ± 4.8	$\mathbf{91.7 \pm 2.9}$	84.4 ± 1.8
synthetic + real	5000	84.6 ± 4.2	86.9 ± 3.6	85.7 ± 2.1	76.9 ± 5.2	91.4 ± 3.0	84.2 ± 2.2
synthetic + real	10000	84.2 ± 2.8	$\mathbf{88.5 \pm 2.9}$	$\mathbf{86.3 \pm 1.8}$	$\mathbf{79.1 \pm 4.7}$	91.0 ± 2.6	$\mathbf{85.1 \pm 1.9}$

TABLE 14
Mean test performance of the 20 runs trained on *train-50* with the optimized hyperparameters

		ADNI			AIBL		
image type	synthetic images	sensitivity	specificity	balanced accuracy	sensitivity	specificity	balanced accuracy
real	-	75.4 ± 5.0	75.5 ± 5.3	75.5 ± 2.7	68.6 ± 8.5	82.6 ± 4.2	75.6 ± 4.1
real (high-resolution)	-	73.6 ± 6.2	70.6 ± 5.9	72.1 ± 3.1	57.8 ± 12.3	84.6 ± 4.2	71.2 ± 5.1
synthetic	500	75.8 ± 3.0	77.6 ± 5.3	76.7 ± 2.8	73.2 ± 9.0	$\mathbf{83.6 \pm 4.0}$	78.4 ± 4.0
synthetic	1000	76.7 ± 4.6	78.5 ± 4.9	$\mathbf{77.6 \pm 3.7}$	78.7 ± 7.5	83.2 ± 4.8	80.9 ± 4.3
synthetic	2000	73.9 ± 3.6	$\mathbf{79.8 \pm 4.0}$	76.8 ± 3.0	78.2 ± 6.9	82.4 ± 3.7	80.3 ± 3.5
synthetic	3000	74.4 ± 6.1	79.8 ± 4.9	77.1 ± 4.0	76.4 ± 10.1	82.4 ± 4.3	79.4 ± 4.7
synthetic	5000	77.1 ± 4.5	77.4 ± 5.2	77.2 ± 2.1	81.1 ± 5.9	82.0 ± 3.9	$\mathbf{81.5 \pm 2.6}$
synthetic	10000	$\mathbf{77.5 \pm 5.3}$	77.3 ± 4.7	77.4 ± 3.1	$\mathbf{81.7 \pm 5.4}$	79.7 ± 4.1	80.7 ± 2.9
synthetic + real	500	73.2 ± 4.2	78.0 ± 3.3	75.6 ± 2.5	69.2 ± 9.4	$\mathbf{82.7 \pm 4.1}$	76.0 ± 4.2
synthetic + real	1000	76.1 ± 5.3	$\mathbf{79.5 \pm 2.9}$	77.8 ± 2.3	79.3 ± 5.8	82.5 ± 4.2	80.9 ± 3.2
synthetic + real	2000	75.2 ± 3.8	78.6 ± 4.4	76.9 ± 2.4	77.8 ± 8.8	82.2 ± 4.5	80.0 ± 3.6
synthetic + real	3000	76.5 ± 3.8	79.2 ± 4.2	77.8 ± 1.9	80.9 ± 7.9	81.4 ± 4.2	81.2 ± 3.7
synthetic + real	5000	77.1 ± 3.7	76.7 ± 4.1	76.9 ± 2.5	80.7 ± 6.1	81.2 ± 3.7	80.9 ± 2.7
synthetic + real	10000	$\mathbf{77.8 \pm 4.6}$	78.2 ± 4.9	$\mathbf{78.0 \pm 2.1}$	$\mathbf{81.7 \pm 4.9}$	81.9 ± 4.6	$\mathbf{81.9 \pm 2.2}$

TABLE 15
Mean test performance of the 20 runs trained on *train-full* with the optimized hyperparameters

		ADNI			AIBL		
image type	synthetic images	sensitivity	specificity	balanced accuracy	sensitivity	specificity	balanced accuracy
real	-	82.5 ± 4.2	88.5 ± 6.6	85.5 ± 2.4	75.1 ± 8.4	88.7 ± 9.0	81.9 ± 3.2
real (high-resolution)	-	82.6 ± 4.5	88.9 ± 6.3	85.7 ± 2.5	78.9 ± 5.4	89.9 ± 4.0	84.4 ± 1.7
synthetic	500	81.7 ± 3.6	90.5 ± 3.9	86.1 ± 1.4	75.5 ± 7.1	89.8 ± 4.3	82.6 ± 2.9
synthetic	1000	82.8 ± 3.4	90.0 ± 4.0	86.4 ± 2.1	76.8 ± 4.5	91.5 ± 2.5	84.2 ± 1.7
synthetic	2000	81.3 ± 2.8	91.2 ± 2.8	86.2 ± 1.7	76.2 ± 6.7	$\mathbf{92.2 \pm 3.6}$	84.2 ± 2.6
synthetic	3000	82.2 ± 4.9	90.6 ± 4.5	86.4 ± 2.0	77.7 ± 6.3	90.8 ± 4.4	84.3 ± 2.0
synthetic	5000	80.6 ± 3.4	$\mathbf{91.6 \pm 2.5}$	86.1 ± 1.9	75.3 ± 5.4	92.4 ± 2.5	83.8 ± 2.0
synthetic	10000	$\mathbf{84.0 \pm 3.8}$	89.1 ± 3.1	$\mathbf{86.5 \pm 1.7}$	$\mathbf{79.2 \pm 5.2}$	90.1 ± 3.7	$\mathbf{84.7 \pm 2.3}$
synthetic + real	500	82.3 ± 2.3	89.8 ± 2.7	86.0 ± 1.8	74.9 ± 5.0	91.4 ± 2.6	83.2 ± 2.4
synthetic + real	1000	82.5 ± 3.3	90.5 ± 4.1	86.5 ± 1.9	76.4 ± 5.6	91.0 ± 3.4	83.7 ± 2.0
synthetic + real	2000	$\mathbf{83.1 \pm 4.2}$	$\mathbf{91.3 \pm 3.2}$	$\mathbf{87.2 \pm 1.7}$	76.0 ± 4.7	92.0 ± 2.4	84.0 ± 2.0
synthetic + real	3000	81.3 ± 3.7	90.4 ± 3.4	85.8 ± 2.6	74.9 ± 7.3	92.3 ± 2.6	83.6 ± 3.2
synthetic + real	5000	81.9 ± 3.5	90.9 ± 2.5	86.4 ± 1.3	74.1 ± 4.9	$\mathbf{92.9 \pm 1.9}$	83.5 ± 2.2
synthetic + real	10000	82.2 ± 3.4	91.2 ± 3.6	86.7 ± 1.8	$\mathbf{76.4 \pm 4.2}$	92.1 ± 2.1	$\mathbf{84.3 \pm 1.8}$

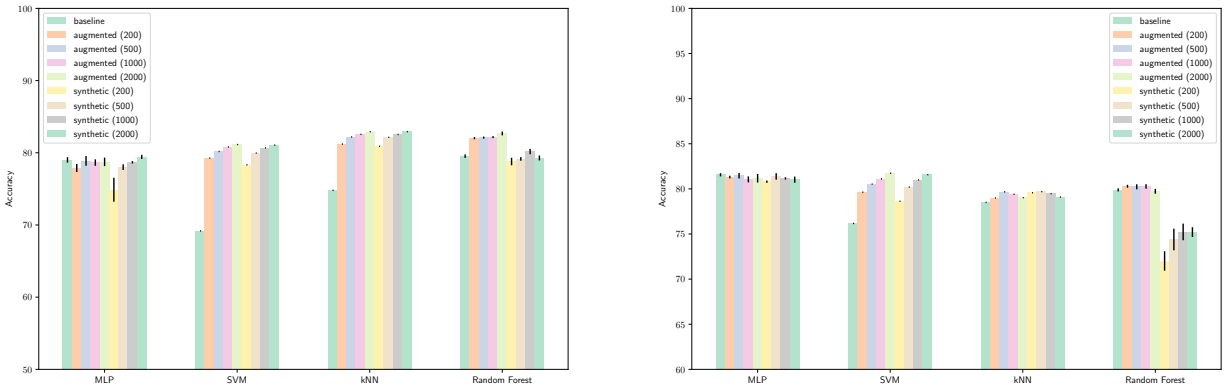

(a) *reduced* EMNIST (b) *reduced* FashionMNIST

Fig. 9. Evolution of the accuracy of 4 benchmark classifiers on the *reduced* EMNIST data set (left) and the *reduced* Fashion data set (right). Stochastic classifiers are trained with 5 independent runs and we report the mean accuracy and standard deviation on the test set.

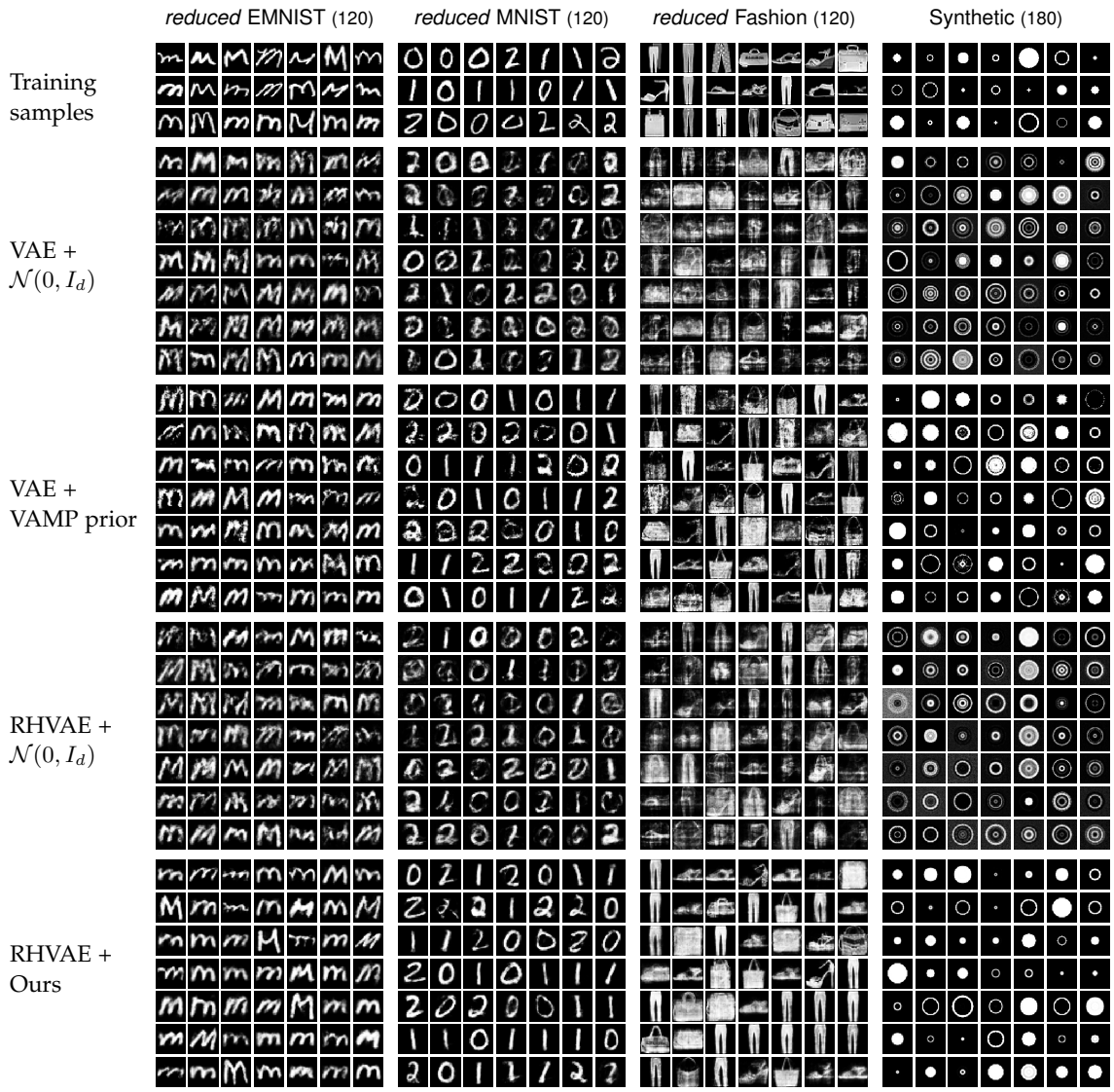

Fig. 10. Comparison of 4 sampling methods on *reduced* EMNIST (120 letters *M*), *reduced* MNIST, *reduced* FashionMNIST and the synthetic data sets in higher dimensional latent spaces (dimension 10). From top to bottom: 1) samples extracted from the training set; 2) samples generated with a Vanilla VAE and using the prior ($\mathcal{N}(0, I_d)$); 3) from the VAMP prior VAE ; 4) from a RHVAE and the *prior-based* generation scheme and 5) from a RHVAE and using the proposed method. All the models are trained with the same encoder and decoder networks and identical latent space dimension. An early stopping strategy is adopted and consists in stopping training if the ELBO does not improve for 20 epochs. The number of training samples is noted between parenthesis.

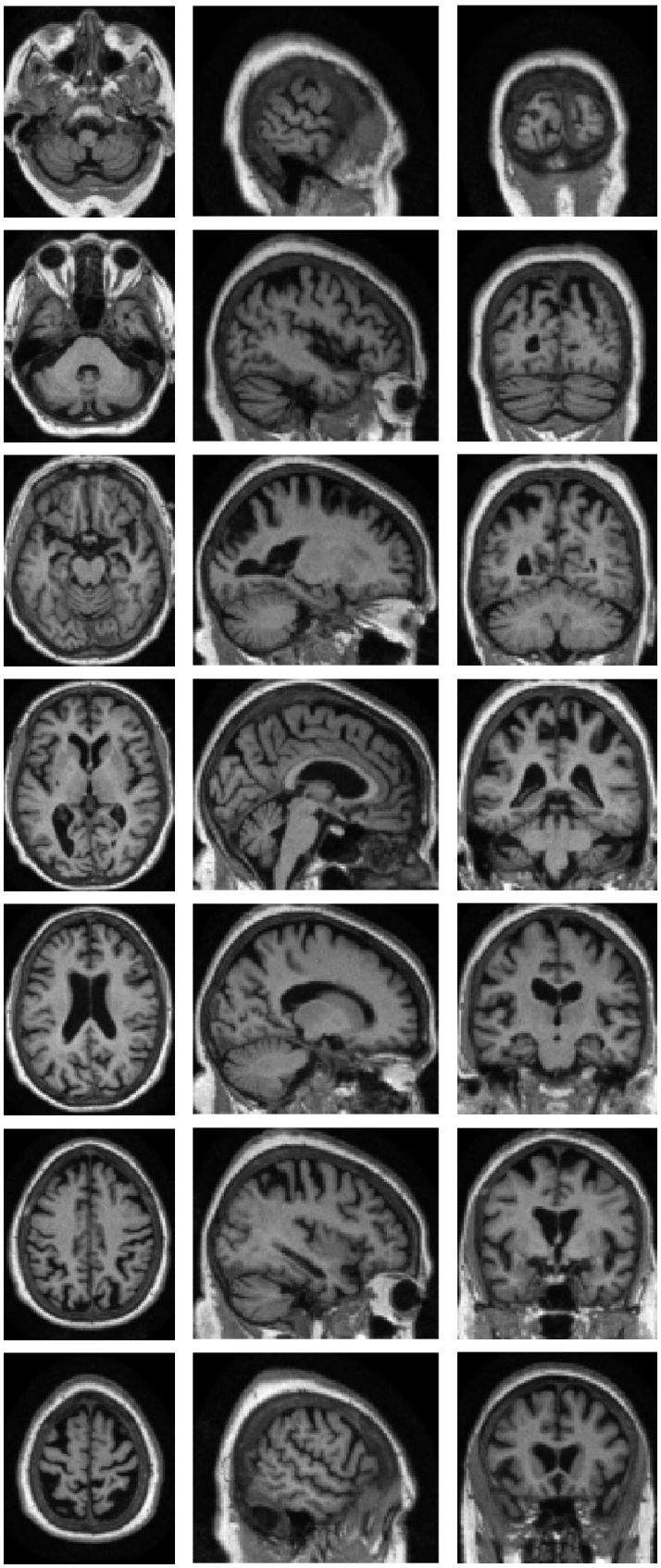

Fig. 11. Several slices of a generated image. The model is trained on the AD class of *train-50* (*i.e.* 50 images of AD patients)

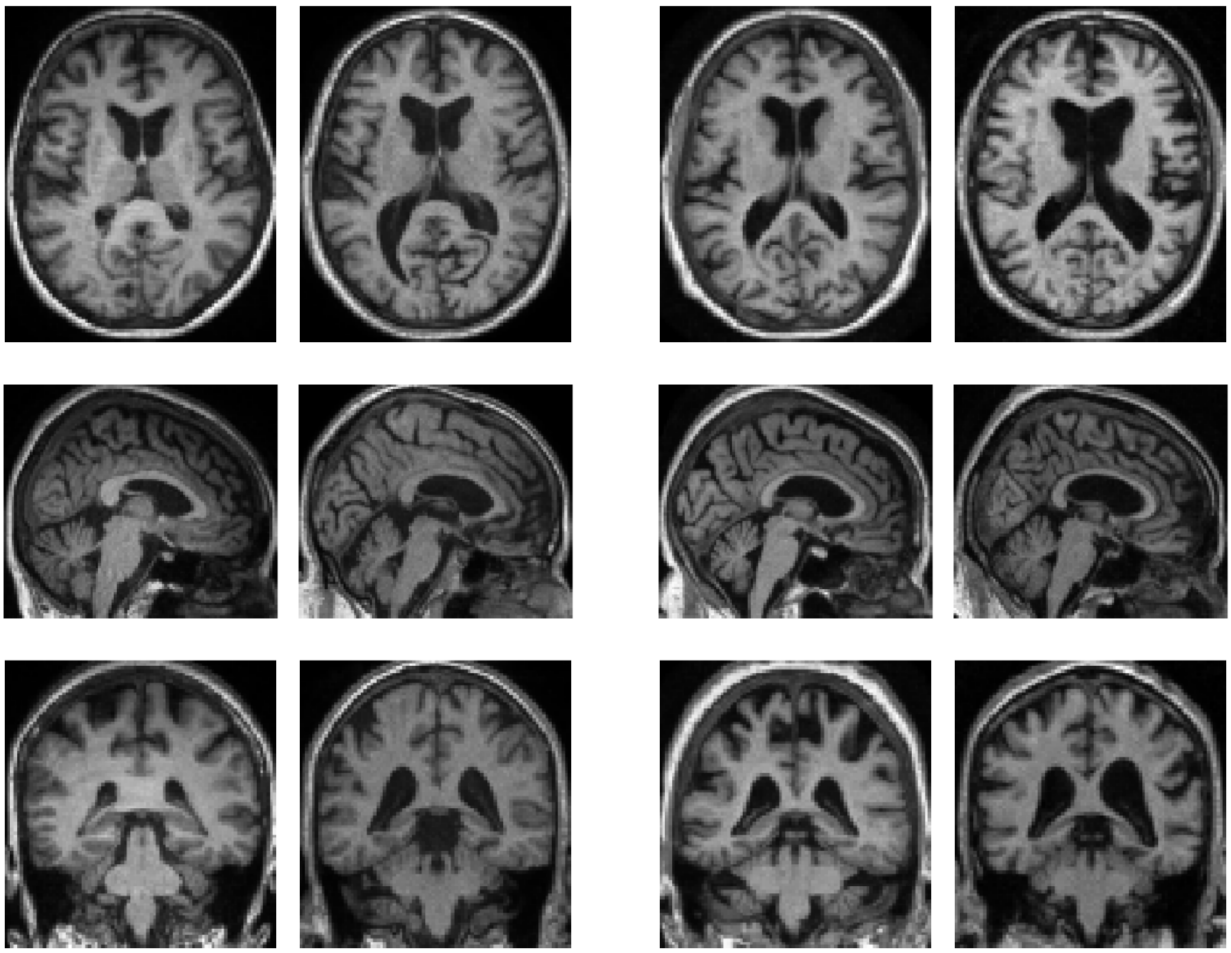

Fig. 12. Images generated by our method when trained on *train-50*. *Left*: CN generated patients. *Right*: AD generated patients.